

Tuning Frictional Properties of Kirigami Altered Graphene Sheets using Molecular Dynamics and Machine Learning

Designing a Negative Friction Coefficient

Mikkel Metzsch Jensen



Thesis submitted for the degree of
Master in Computational Science: Materials Science
60 credits

Department of Physics
Faculty of mathematics and natural sciences

UNIVERSITY OF OSLO

Spring 2023

Tuning Frictional Properties of Kirigami Altered Graphene Sheets using Molecular Dynamics and Machine Learning

Designing a Negative Friction Coefficient

Mikkel Metzsch Jensen



© 2023 Mikkel Metzsch Jensen

Tuning Frictional Properties of Kirigami Altered Graphene Sheets using Molecular Dynamics and Machine Learning

<http://www.duo.uio.no/>

Printed: Reprocentralen, University of Oslo

Abstract

Abstract.

Acknowledgments

Acknowledgments.

List of Symbols

F_N Normal force (normal load)

Acronyms

AFM atomic force microscope. 20, 21, 22, 24

FFM friction force microscopes. 20, 21, 22, 24

FK Frenkel-Kontorova. 11, 16, 18, 19, 20, 22, 23, 24

FKT Frenkel–Kontorova–Tomlinson. 11

GS ground state. 17, 18

MD molecular dynamics. 2, 3, 11, 12, 14, 22, 23, 24

ML machine learning. 2, 3

PT Prandtl–Tomlinson. 11

SFA Surface forces apparatus. 21, 22

SFM scanning force microscopies. 20

SPM scanning probe microscopy. 20

Contents

1	Introduction	1
1.1	Motivation	1
1.2	Goals	3
1.3	Contributions	3
1.4	Thesis structure	3
I	Background Theory	5
2	Friction	7
2.1	Friction across scales	7
2.2	Macroscale	7
2.2.1	Amontons' law	8
2.3	Microscopic scale	9
2.3.1	Surface roughness — Asperity theories	9
2.4	Nanoscale - Atomic scale	10
2.4.1	Prandtl-Tomlinson	11
2.4.1.1	Thermal activation	12
2.4.1.2	Sliding speed	14
2.4.1.3	Mass	15
2.4.1.4	Friction Regimes: Smooth Sliding, Single Slip, and Multiple Slip	15
2.4.1.5	2D nature	16
2.4.2	Frenkel-Kontorova	16
2.4.2.1	Commensurability	17
2.4.2.2	Kinetic friction	19
2.4.3	Dependence	20
2.4.4	Experimental procedures	20
2.4.4.1	Scanning Probe Microscopy	20
2.4.4.2	Surface Force Apparatus (SFA)	21
2.4.5	Numerical procedures	21
2.5	Expected frictional properties of graphene	21
2.6	Research questions	26
3	Molecular Dynamics	27
3.1	Potentials	27
3.1.1	General formulation of potentials (?)	27
3.1.2	Lennard Jones	27
3.1.3	Stillinger weber	28
3.1.4	Tersoff	29
3.2	Integration	30
3.2.1	Velocity Verlet	31
3.3	Thermostats	31
3.3.1	Langevin thermostat	32
3.3.2	Implementing Langevin	34

3.4	MD limitations (?)	34
3.5	LAMMPS	34
II	Simulations	35
4	Pilot study	37
4.1	Friction simulation parameters	37
4.1.1	Pressure reference for normal load domain	39
4.2	Single friction simulation analysis	40
4.2.1	Force oscillations	40
4.2.2	Decompositions	41
4.2.3	Center of mass path	42
4.3	Defining metrics for dynamic and static friction	43
4.3.1	Dynamic friction	43
4.3.2	Static friction	44
4.4	Out of plane buckling	45
4.5	Investigating selected parameters	47
4.6	Normal force and stretch dependencies	49
4.6.1	Contact area	50
4.6.2	Stretch	50
4.6.3	Normal force	52
4.7	Computational cost	53
Appendices		55
Appendix A		57
Appendix B		59
Appendix C		61

Chapter 1

Introduction

Structure of Motivation section:

1. Introduce and motivate friction broadly.
2. Motives for friction control using a grasping robot as example.
3. Analog to gecko feet where adhesive properties are turned on and off.
4. Interest in origin of friction through nanoscale studies which further motivates the use of MD.
5. Intro to metamaterials and the use of kirigami designs,
6. How to optimize kirigami designs with reference to Hanakata and motivating the use of ML.
7. Out-of-plane buckling motivates the use of kirigami for frictional properties.

Does some of the latter paragraphs belong to the approach section?

1.1 Motivation

Friction is a fundamental force that takes part in most of all interactions with physical matter. Even though the everyday person might not be familiar with the term *friction* we recognize it as the inherent resistance to sliding motion. Some surfaces appear slippery and some rough, and we know intuitively that sliding down a snow covered hill is much more exciting than its grassy counterpart. Without friction, it would not be possible to walk across a flat surface, lean against the wall without falling over or secure an object by the use of nails or screws [p. 5] [1]. It is probably safe to say that the concept of friction is integrated in our everyday life to such an extent that most people take it for granted. However, the efforts to control friction dates back to the early civilization (3500 B.C.) with the use of the wheel and lubricants to reduce friction in translational motion [2]. Today, friction is considered a part of the wider field *tribology* derived from the Greek word *Tribos* meaning “rubbing” and includes the science of friction, wear and lubrication [2]. The most compelling motivation to study tribology is ultimately to gain full control of friction and wear for various technical applications. Especially, reducing friction is of great interest as this has tremendous advantages for energy efficiency. It has been reported that tribological problems have a significant potential for economic and environmental improvements [3]:

“On global scale, these savings would amount to 1.4% of the GDP annually and 8.7% of the total energy consumption in the long term.” [4].

On the other hand, the reduction of friction is not the only sensible application for tribological studies. Controlling frictional properties, besides minimization, might be of interest in the development of a grasping robot where a finetuned object handling is required. While achieving a certain “constant” friction response is readily obtained through appropriate material choices during manufacturing, we are yet to unlock the capabilities to alter friction dynamically on the go. One example from nature inspiring us to think along these lines are the gecko feet. More precisely, the Tokay gecko has received a lot of attention in scientific studies aiming to unravel the underlying

mechanism of its “toggable” adhesion properties. Although geckos are able to produce large adhesive forces, they retain the ability to remove their feet from an attachment surface at will [5]. This makes the gecko able to achieve a high adhesion on the feet when climbing a vertical surface while lifting it for the next step remains relatively effortless. For a grasping robot we might consider an analog frictional concept of a surface material that can change from slippery to rough on demand depending on specific tasks.

In the recent years an increasing amount of interest has gone into the studies of the microscopic origin of friction, due to the increased possibilities in surface preparation and the development of nanoscale experimental methods. Nano-friction is also of great concern for the field of nano-machining where the frictional properties between the tool and the workpiece dictates machining characteristics [3]. With concurrent progress in computational power and development of Molecular Dynamics (MD), numerical investigations serve as an extremely useful tool for getting insight into the nanoscale mechanics associated with friction. This simulation based approach can be considered as a “numerical experiment” enabling us to create and probe a variety of high complexity systems which are still out of reach for modern experimental methods.

In materials science such MD-based numerical studies have been used to explore the concept of so-called *metamaterials* where material compositions are designed meticulously to enhance certain physical properties [6][7][8][9][10][11]. This is often achieved either by intertwining different material types or removing certain regions completely. In recent papers by Hanakata et al. [6](2018) [7](2020) numerical studies have showcased that mechanical properties of a graphene sheet, in this case yield stress and yield strain, can be altered through the introduction of so-called *kirigami* inspired cuts into the sheet. Kirigami is a variation of origami where the paper is cut additionally to being folded. While these methods originate as an art form, aiming to produce various artistic objects, they have proven to be applicable in a wide range of fields such as optics, physics, biology, chemistry and engineering [12]. Various forms of stimuli enable direct 2D to 3D transformations through folding, bending, and twisting of microstructures. While original human designs have contributed to specific scientific applications in the past, the future of this field is highly driven by the question of how to generate new designs optimized for certain physical properties. However, the complexity of such systems and the associated design space makes for seemingly intractable problems ruling out analytic solutions.

Earlier architecture design approaches such as bioinspiration, looking at gecko feet for instance, and Edisonian, based on trial and error, generally rely on prior knowledge and an experienced designer [9]. While the Edisonian approach is certainly more feasible through numerical studies than real world experiments, the number of combinations in the design space rather quickly becomes too large for a systematic search, even when considering the simulation time on modern day hardware. However, this computational time constraint can be relaxed by the use of machine learning (ML) which have proven successful in the establishment of a mapping from the design space to physical properties of interest. This gives rise to two new styles of design approaches: One, by utilizing the prediction from a trained network we can skip the MD simulations all together resulting in an *accelerated search* of designs. This can be further improved by guiding the search accordingly to the most promising candidates, as for instance done with the *genetic algorithm* which suggest new designs based on mutation and crossing of the best candidates so far. Another, even more sophisticated approach, is through generative methods such as *Generative Adversarial Networks* (GAN). By working with a so-called *encoder-decoder* network structure, one can build a model that reverses the prediction process. That is, the model predicts a design from a set of physical target properties. In the papers by Hanakata et al. both the *accelerated search* and the *inverse design* approach was proven successful to create novel metamaterial kirigami designs with the graphene sheet.

Hanakata et al. attributes the variety in yield properties to the non-linear effects arising from the out-of-plane buckling of the sheet. Since it is generally accepted that the surface roughness is of great importance for frictional properties it can be hypothesized that the kirigami cut and stretch procedure can also be exploited for the design of frictional metamaterials. For certain designs we might hope to find a relationship between stretching of the sheet and frictional properties. If significant, this could give rise to a variability of the friction response beyond manufacturing material choice. For instance, the grasping robot might apply such a material as artificial skin for which stretching or relaxing of the surface could result in a changeable friction strength; Slippery and smooth when in contact with people and rough and firmly gripping when moving heavy objects. In addition, a possible coupling between stretch and the normal load through a nanomachine design would allow for an altered friction coefficient. This invites the idea of non-linear friction coefficients which might in theory also take on negative values given the right response from stretching. The latter would constitute an extremely rare property. This has (**only?**) been reported indirectly for bulk graphite by Deng et al. [13] where the friction kept increasing during the unloading phase. **Check for other cases and what I can really say here.**

To the best of our knowledge, kirigami has not yet been implemented to alter the frictional properties of a nanoscale system. In a recent paper by Liefferink et al. [14](2021) it is reported that macroscale kirigami can be used to dynamically control the macroscale roughness of a surface through stretching which was used to change the frictional coefficient by more than one order of magnitude. This supports the idea that kirigami designs can in fact be used to alter friction, but we believe that taking this concept to the nanoscale regime would involve a different set of underlying mechanisms and thus contribute to new insight in this field.

1.2 Goals

In this thesis we investigate the possibility to alter and control the frictional properties of a graphene sheet through application of kirigami inspired cuts and stretching of the sheet. With the use of MD simulations we evaluate the friction properties under different physical conditions in order to get insight into the prospects of this field. By evaluating variations of two kirigami inspired patterns and a series of random walk generated patterns we create a dataset containing information of the frictional properties associated with each design under different load and stretch conditions. We apply ML to the dataset and use an accelerated search approach to optimize for different properties of interest. The subtask of the thesis are presented more comprehensively in the following.

1. Define a sheet indexing that allows for a unique mapping of patterns between a hexagonal graphene lattice representation to a matrix representation suited for numerical analysis.
2. Design a MD simulation procedure to evaluate the frictional properties of a given graphene sheet under specified physical conditions such as load, stretch, temperature etc.
3. Find and implement suitable kirigami patterns which exhibit out-of-plane buckling under tensile load. This includes the creation of a framework for creating variations within each pattern class. Additionally create a procedure for generating different styles of random walk patterns.
4. Perform a pilot study of a representative subset of patterns in order to determine appropriate simulation parameters to use for the further study along with an analysis of the frictional properties shown in the subset.
5. Create a dataset consisting of the chosen kirigami variations and random walk patterns and analyse data trends.
6. Train a neural network to map from the design space to physical properties such as mean friction, maximum friction, contact area etc. and evaluate the performance.
7. Perform an accelerated search optimizing for interesting frictional properties using the ML model. This should be done both through the pattern generation procedures and by following a genetic algorithm approach.
8. Use the most promising candidates from the accelerated search to investigate the prospects of creating a nanomachine setup which exhibits a negative friction coefficient.
9. Study certain designs of interest with the scope of revealing underlying mechanism. This includes simple correlation analysis but also a visualization of feature and gradient maps of the ML network.

Is the list of subtask too specific? Some of the details here might be better suited for the thesis structure section.

1.3 Contributions

What did I actually achieve

1.4 Thesis structure

How is the thesis structured.

Part I

Background Theory

Chapter 2

Friction

Friction plays a central role for the topic of this thesis, as this is the key concept that we want to explore through design of microstructures. In this chapter we review relevant theoretical understanding and highlight the theoretical expectations for our study.

Friction is a part of the wider field tribology which includes the study of friction, wear and lubrication between two surfaces in relative motion [1, p. 1]. In this thesis we will only concern ourselves with so-called wearless dry friction. That is, without any use of lubrication and without any resulting wear of the contacting surfaces.

2.1 Friction across scales

Tribological systems take place across a broad range of time and length scales, ranging from geological stratum layers involved in earthquakes [3] to microscopic atomistic processes, as in the gliding motion of a nanocluster of a nanomotor [15]. This vast difference in scale gives rises to different frictional mechanism being dominating at different scales. On a macro scale the system is usually subject to relatively high load and sliding speed leading to high contact stress and wear. On the other hand, the micro-/nanoscale regime occupies the opposite domain operating under relatively small load and sliding speed with negligible wear [3] [2, p. 5]. While macroscale friction is often reduced into a few variables such as load, material type, sliding speed and surface roughness it is clear that the micro-/nanoscale friction cannot be generalized under such a simple representation. On the micro-/nanoscale the tribological properties are dominated by surface properties which will introduce an additional sensitivity to variables such as temperature, humidity and even sliding history. The works of Bhushan and Kulkarni [16, (1996)] showed that the friction coefficient decreased with scale even though the materials used was unchanged. This reveals an intrinsic relationship between friction and scale as the contact condition is altered.

The phenomenological descriptions of macroscale friction cannot yet be derived from the fundamental atomic principles, and bridging the gap between different length scales in tribological systems remains an open challenge [15]. Hence, the following sections will be organized into macro-, micro- and nanoscale representing the theoretical understanding governing each scale regime. While our study of the graphene sheet is based on a nanoscale perspective the hypothesizing about application possibilities will eventually draw upon a macroscale perspective as well. Thus, we argue that a brief theoretical introduction to all three major scales is suitable for a more complete interpretation of the findings in this thesis.

2.2 Macroscale

Our working definition of the *macroscale* is everything on the scale of visible objects. This is usually denoted to the size of millimeters 10^{-3} m and above. Most importantly, we want to make a distinction to the microscale,

where the prefix indicates the size of micrometers m^{-6} . Hence, we essentially consider everything larger than *micro* to belong to the macroscale¹.

2.2.1 Amontons' law

In order to start and keep a solid block moving against a solid surface we must overcome certain frictional forces F_{fric} [1]. The static friction force F_s corresponds to the minimum tangential force required to initiate the sliding while the kinetic friction force F_k corresponds to the tangential force needed to sustain such a sliding at steady speed. The work of Leonardo da Vinci (1452–1519), Guillaume Amontons (1663–705) and Charles de Coulomb (1736–1806) all contributed to the empirical law, commonly known as *Amontons' law*, which serves as a common base for macroscale friction. Amontons' law states that the frictional forces is entirely independent of contact area and sliding velocity. Instead, it relies only on the normal force F_N , acting perpendicular to the surface, and the material specific friction coefficient μ as

$$F_{\text{fric}} = \mu F_N. \quad (2.1)$$

Notice that the term *Normal force* is often used interchangeably with *load* and *normal load* although the latter two terms refer to the applied force, “pushing” the object into the surface, and the first is the reaction force acting from the surface on the object. In equilibrium, these forces are equal in magnitude and hence we will not make a distinction between these terms. On the same note, the frictional force is different from a conventional force which in the Newtonian definition acts on a body from the outside and make it accelerate [17]. Rather than being an independent external force the friction force is an internal *reaction* force opposing the externally applied “sliding” force.

The friction coefficient μ is typically different for the cases of static (μ_s) and kinetic (μ_k) friction, usually both with values lower than one and $\mu_s \geq \mu_k$ in all cases [1, p. 6]. The friction coefficient is taken to be a constant defined by either [17]

$$\mu_1 = \frac{F_{\text{fric}}}{F_N}, \quad (2.2a) \quad \text{or} \quad \mu_2 = \frac{dF_{\text{fric}}}{dF_N}. \quad (2.2b)$$

The first definition Eq. (2.2a) requires zero friction at zero load, i.e. $F_{\text{fric}} = 0$ at $F_N = 0$, while the second definition (Eq. (2.2b)) allows for a finite friction force at zero load since the coefficient is instead given by the slope of the F_{fric} vs. F_N curve. The consequences of the two different definitions are illustrated in Fig. 2.1. Usually the friction force is not zero under zero load (red curve: Linear + shift) due to adhesive forces **source**, which constitutes an additional constant added to Amontons' law in Eq. (2.1). Using the first definition (Eq. (2.2a)) would make the friction coefficient diverge for low load as illustrated in Fig. 2.1, and thus we will use the second definition (Eq. (2.2b)) moving forward. This also allows for a better interpretation in cases where Amontons' law does not hold true and the friction force change non-linear with load (Purple curve in Fig. 2.1).

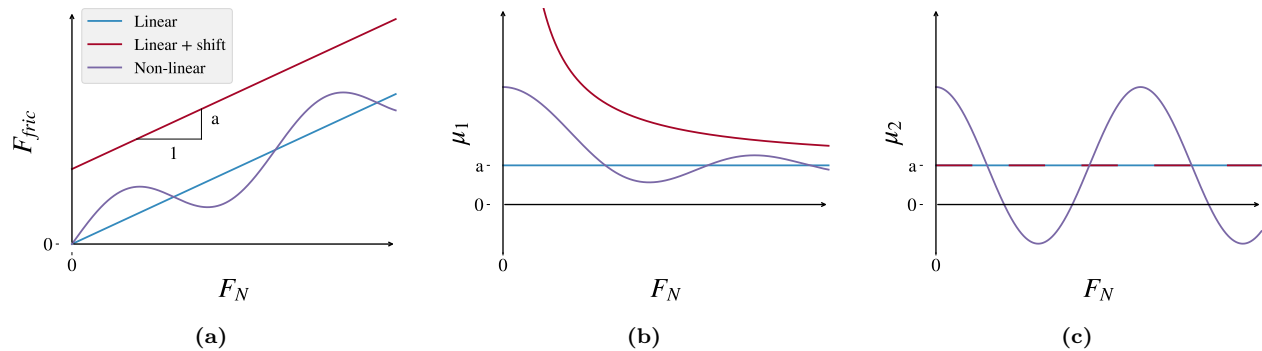


Figure 2.1: CAPTION

¹The width of a human hair is often used as a reference for the limit of human perception. Since the width of a human hair is on the length scale 10^{-5} to 10^{-4} m we find that this definition of the lower perceptual limit aligns rather well with the transition from macro- to microscale.

Although Amontons' law has been successful in its description of the majority of rubbing surfaces, involving both dry and lubricated, ductile and brittle and rough and smooth (as long as they are not adhesive) surfaces [17], it has its limitations. It is now known that Eq. (2.1) is not valid over a large range of loads and sliding velocities and that it completely breaks down for atomically smooth surfaces in strongly adhesive contact [17]. The independency of sliding velocity disappears at low velocities as thermal effects becomes important and for high velocities due to inertial effects [1, pp. 5-6]. For the case of static friction, it was discovered to be dependent on the so-called contact history with increasing friction as the logarithm of time of stationary contact.

In cases where amontons' law breaks down we might still use the conceptual definition of the friction coefficient as defined by (Eq. (2.2b)). Especially, in the context of achieving negative friction coefficients (in certain load ranges) we would refer to this definition, since (Eq. (2.2a)) would imply a truly unphysical situation of the frictional force acting in the same direction as the sliding motion. This would accelerate the object indefinitely².

Due to the emperical foundation of Amontons' law it does not provide any physical insight into the underlying mechanisms of friction. However, as we will later discuss in more detail, we can understand the overall phenomena of friction through statistical mechanics by the concept of *equipartition of energy* [15]. A system in equilibrium has its kinetic energy uniformly distributed among all its degrees of freedom. When a macroscale object is sliding in a given direction it is clearly not in equilibrium since one of its degrees of freedom carries considerable more kinetic energy. Thus, the system will have a tendency to transfer that kinetic energy to the remaining degrees of freedom as heat. This heat will dissipate to the sourroundings and the object will slow down as a result. Hence, we can understand friction simply as the tendency of going toward equilibrium energy equipartitioning among many interacting degrees of freedom [15]. From this point of view it is clear that friction is an inevitable part of contact physics, but even though friction cannot be removed altogether, we are still capable of manipulating it in usefull ways.

The attentive reader might point out that we have already moved the discussion partly into the microscopic regime as *statistical mechanics* generally aim to explain macroscale behaviour by microscopic interactions. In fact, this highlight the nessecity to consider smaller scales in order to achieve a more fundamental understdadning of friction.

2.3 Microscopic scale

Going from a macro- to microscale perspective, to a length scale of order 10^{-6} m, it was realized that most surfaces is in fact rough [18]. The contact between two surfaces consist of numerous smaller contact point, so-called asperities, for which the friction between two opposing surfaces involves interlocking of those asperities as visualized in Fig. 2.2. Small junctions of asperities are formed due to contact pressure and adhesion [3].

In the macroscale perspective of Amonton's law we refer to time- and space-averaged values, i.e. the "apparent" contact area and the average sliding speed [17]. However, microspocially we find the real contact area to be smaller than the macroscale apparent area and the shearing of local microjunctions can happen at large fluctuations or in a stick-slip fashion.

It is generally accepted that friction is caused by two mechanism: mechanical friction and chemical friction [3]. The mechanical friction is the "plowing" of the surface by hard particles or said asperities with an energy loss attributed to deformations of the asperity. While plastic deformations, corresponding to wear, gives rise to an obvious attribution for the energy loss, elastic deformations is also sufficient in explaining energy loss due to phonon excitations. In fact the assumption of plastic deformations has been critizised as this is theorized only to be present in the beginning of a surface contact while it is neglible for prolonged or repeated contact of the same surfaces [19]. That is, when machine parts slide against each other for millions of cycle the plastic deformation would only take place in the beginning for which the system then reaches a steady state with only elastic deformations. The chemical friction arrises from adhesion between microscopic contacting surfaces, with an energy loss attributed to breaking and forming of bonds.

2.3.1 Surface roughness — Asperity theories

Asperity theories are based on the observation that microscopic rough surfaces, with contacting asperities each with a contact area of A_{asp} , will have a true contact area $\sum A_{\text{asp}}$ much smaller than the apperent macrosopic

²You would most likely have a good shot at the Nobel Prize with that paper.

area [3]. The friction force has been shown to be proportional to the true contact area as

$$F_{\text{fric}} = \tau \sum A_{\text{asp}},$$

where τ is an effective shear strength of the contacting bodies. Note that this is still compatible with Amontons' law in Eq. (2.1) by having a linear relationship between the real contact area and the applied load. In Fig. 2.2 we see a visualization on how the contact area might intuitively increase with load as the asperity tips are deformed (plastically or elastically) into broader contact points.

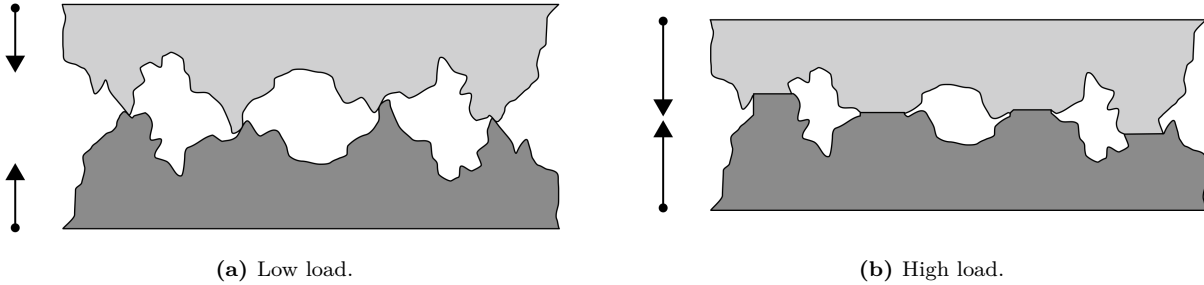


Figure 2.2: Qualitative illustration of the microscopic asperity deformation under increasing load from frame (a) to (b) [20]. While this figure seemingly portrays plastic deformation the concept of increased contact area under increased load applies for elastic deformation as well.

Many studies have focused on single asperity contacts to reveal the relationship between the contact area and load [21][22][23]. By assuming perfectly smooth asperities, with radii of curvature from micrometers all the way down to nanometers, continuum mechanics can be used to predict the deformation of asperities as load is applied. A model for non-adhesive contact between homogenous, isotropic, linear elastic spheres was first developed by Hertz [24], which predicted $A_{\text{asp}} \propto F_N^{2/3}$. Later adhesion effects were included in a number of subsequent models, including Maugis-Dugdale theory [25], which also predicts a sublinear relationship between A_{asp} and F_N . Thus, the common feature of all single-asperity theories is that A_{asp} is a sublinear function of F_N , leading to a similar sublinear relationship for $F_{\text{fric}}(F_N)$, which fails to align with the macroscale observations modelled by Amontons' law (eq. (2.1)).

Concurrently with single-asperity studies, roughness contact theories are being developed [26][27][28][29] to bridge the gap between single asperities and macroscopic contacts [18]. A variety of multi-asperity theories has attempted to combine single asperity mechanics by statistical modelling of the asperity height and spatial distributions [19]. This has led to a partially success in the establishment of a linear relationship between A_{asp} and F_N . Unfortunately, these results are restricted in terms of the magnitude of the load and contact area, where multi-asperity contact models based on the original ideas of Greenwood and Williamson [28] only predicts linearity at vanishing low loads, or Persson [27] which works for more reasonable loads but only up to 10-15 % of the macroscale contact area. However, as the load is further increased all multi-asperity models predict the contact area to fall into the sublinear dependency of normal force as seen for single asperity theories as well [19].

2.4 Nanoscale - Atomic scale

Going from a micro- to a nanoscale, on the order of 10^{-9} m, it has been predicted that continuum mechanics will start to break down [30] due to the discreteness of individual atoms. In a numerical study by Mo et al. [18] (considering asperity radii of 5-30 nm) it has been shown that the asperity area A_{asp} , defined by the circumference of the contact zone, is sublinear with F_N . This is accommodated by the observation that not all atoms within the circumference make chemical contact with the substrate. By modelling the real contact area $A_{\text{real}} = N A_{\text{atom}}$, where N is the amount of atoms within the range of chemical interaction and A_{atom} the associated surface area for an atom, they found a consistent linear relationship between friction and the real contact area. Without adhesive forces this lead to a similar linear relationship $F_{\text{fric}} \propto F_N$, while adding van der Waals adhesion to the simulation gave a sublinear relationship, even though the $F_{\text{fric}} \propto A_{\text{real}}$ was maintained. This result emphasizes that the predictions of continuum mechanics might still apply as the contact area is still

expected to play an important role at the nanoscale for asperity theory. It is simply the definition of the contact area that undergoes a change when transitioning from micro- to nanoscale.

While the study by Mo et al. [18] considers a single asperity on a nanoscale, some models take this even further to what we might denote the atomic-scale. Our system of interest, is an atomically flat graphene sheet imposed on a flat silicon substrate, which lacks the presence of any nanoscale asperities in its initial uncut undeformed state.

In the lack of noteworthy structural asperities, friction can instead be modelled as a consequence of the "rough" potential laid out by the atomic landscape. A series of so-called reduced-order models builds on a simplified system of atomic-scale contact which builds on three essential parts: 1) A periodic potential modelling a rigid crystalline substrate. 2) An interacting particle, or chain of particles, placed in the potential with a spring-like coupling to 3) a moving body moving at steady speed. In figure Fig. 2.3 three of the most common 1D models is displayed which we will address in the following sections. The time-honored Prandtl-Tomlinson (PT) model describes a point-like tip sliding over a space-periodic fixed crystalline surface with a harmonic coupling to the moving body. This is analog to that of an experimental cantilever used for Atomic Force Microscopy which we will introduce in more details in Sec. 2.4.4.1. Further extensions were added in the Frenkel-Kontorova (FK) model by substituting the tip with a chain of harmonic coupled atoms dragged from the end, and finally combined in the Frenkel-Kontorova-Tomlinson (FKT) with the addition of a harmonic coupling for each of the atoms in the chain with the moving body. While these models cannot provide the same level of details as atomistic simulations such as MD it enables investigation of atomic friction under most conditions, some of which are inaccessible to MD [31]. This makes for an understanding of the individual parameters and mechanisms affecting friction as a whole.

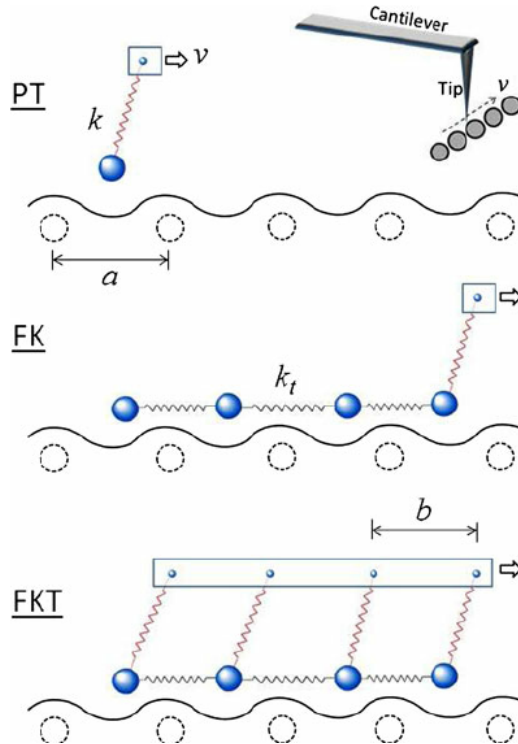


Figure 2.3: [Temporary] figure from [31]

2.4.1 Prandtl–Tomlinson

We start with the Prandtl–Tomlinson (PT) [31, pp. 2, 3] with added thermal activation as proposed by Gnecco et al. [32]. For the theoretical foundation of this section we generally refer to [31].

The 1D PT model assumes a single ball-tip coupled harmonically to a support moving at constant speed which makes the tip slide along the rigid substrate. The interaction between tip and substrate is modelled as a sinusoidal corrugation potential mimicking the periodicity found in a crystalline substrate. The total potential

energy is given as

$$V(x, t) = \frac{1}{2}K(vt - x)^2 - \frac{1}{2}U_0 \cos\left(\frac{2\pi x}{a}\right). \quad (2.3)$$

The first term describes the harmonic coupling at time t , with spring constant K , between the tip at position x and the moving body at position vt given by its constant speed v . The second term describes the corrugation potential with amplitude U_0 and period a representing the lattice spacing of the substrate. The dynamics of the tip can be described by the Langevin equations

$$m\ddot{x} + m\mu\dot{x} = -\frac{\partial V(x, t)}{\partial x} + \xi(t), \quad (2.4)$$

Match notation with later use.

where m is the mass of the tip, μ the viscous friction and $\xi(t)$ the thermal activation term. The equation is solved for tip position x and the friction force is retrieved as the force acting on the moving body

$$F_{\text{fric}} = K(vt - x).$$

The governing equation Eq. (2.4) belongs to a family of stochastic differential equations composed of deterministic dynamics and stochastic processes. In this case the deterministic term is the viscous friction to resist the movement of the tip and the force acting from the corrugation potential. The stochastic term is a random force field modelling thermal noise according to the fluctuation–dissipation relation. Thus, there is no single path but rather multiple paths the tip can take. While the Langevin equations is one of the most common ways to handle thermal activation other methods exist to solve this problem such as Monte Carlo sampling methods. We omit the numerical scheme for solving this and refer to a more in depth discussion of the Langevin equations with respect to MD simulations in Sec. 3.3.1.

2.4.1.1 Thermal activation

The solving of the Langevin equations, as opposed to Newton's equation of motion, introduces the thermal effects to the solution. Generally when the energy barrier comes close to $k_B T$ (0.026 eV at room temperature) thermal effects can not be neglected. In the case of a single asperity contact the energy barrier is on the order 1 eV which make thermal activation significant [31]. Due to the moving body travelling at constant speed the potential energy will increase steadily. Without any temperature $T = 0$ the slip will only occur when the energy barrier between the current potential well (i) and the adjacent (j) is zero $\Delta V_{i \rightarrow j} = 0$. However, in the presence of temperature we get thermal activation, meaning that the tip can slip to the next potential well sooner $\Delta V_{i \rightarrow j} > 0$. Provided that the sliding speed is slow enough (**Why and how slow**) the transition rate κ for a slip from the current to the next well is given by

$$\kappa = f_0 e^{-\Delta V/k_B T}, \quad (2.5)$$

with ΔV being the energy barrier and f_0 the attempt rate. The attempt rate following Kramer's rate theory [33] is related to **...** and can be thought of as the frequency which the tip "attempts" to overcome the barrier (**a bit handwavy**). Sec. 2.4.1.1 resembles the microstate probability in the canonical ensemble with f_0 in place of the inverse partition function Z^{-1} which also serves as a great explanation for the need of this factor. The probability p_i that the tip occupies the current well i relative to the adjacent well j , as illustrated in Fig. 2.4 is governed by

$$\frac{dp_i}{dt} = -\kappa_{i \rightarrow j} p_i + \kappa_{j \rightarrow i} p_j.$$

This probability is related to temperature, speed and mass through .

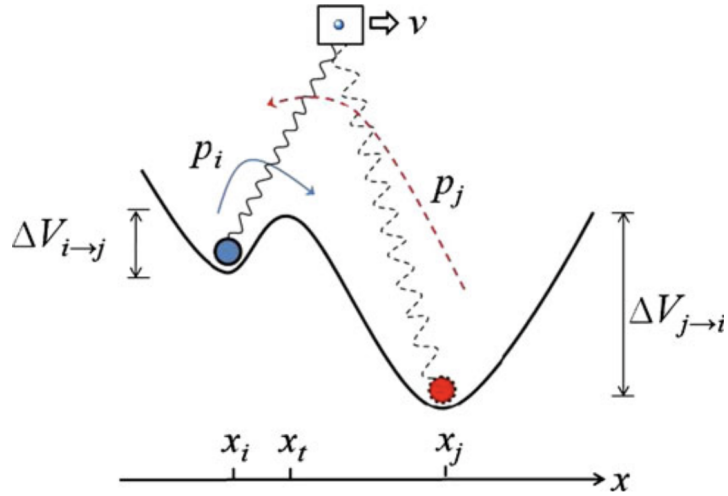


Fig. 3 An illustration of slip between two adjacent energy minima. p_i is the probability of the tip residing in the current potential well, i , where the energy barrier is $\Delta V_{i \rightarrow j}$. p_j is the probability of the tip residing at the next minima, j , where $\Delta V_{j \rightarrow i}$ is the corresponding energy barrier

Figure 2.4: [Temporary] figure from [31]

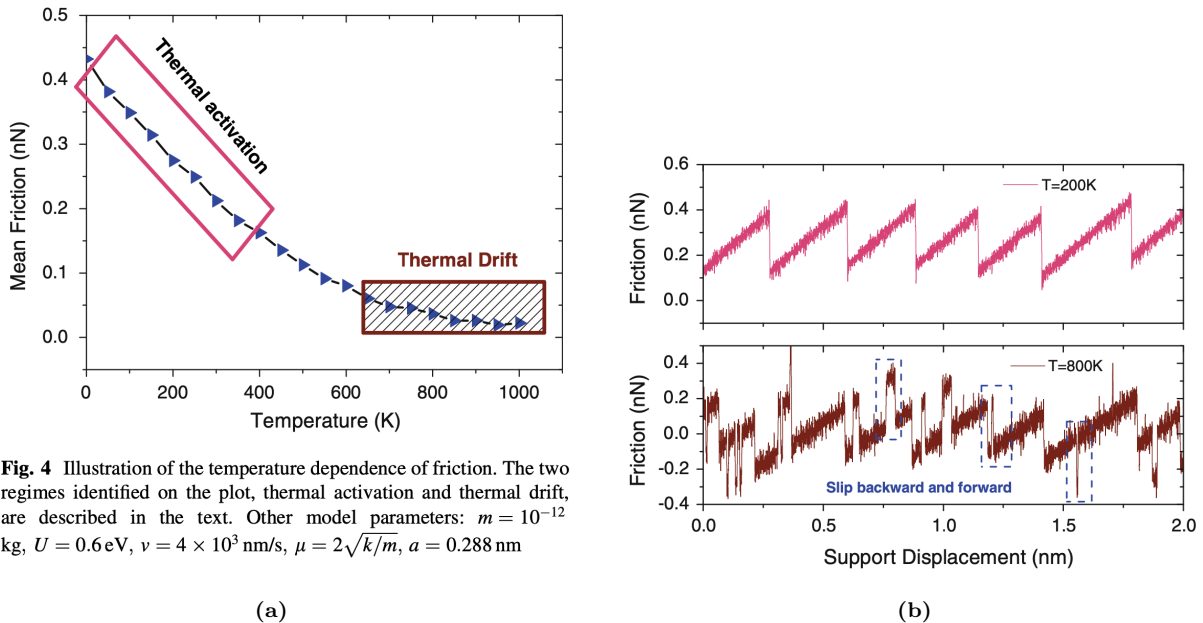


Fig. 4 Illustration of the temperature dependence of friction. The two regimes identified on the plot, thermal activation and thermal drift, are described in the text. Other model parameters: $m = 10^{-12}$ kg, $U = 0.6$ eV, $v = 4 \times 10^3$ nm/s, $\mu = 2\sqrt{k/m}$, $a = 0.288$ nm

Figure 2.5: [Temporary] figures from [31]

Generally, there exist two temperature regimes in the model: Thermal activation (low temperature) and thermal drift (high temperature) as shown in Fig. 2.5. At lower temperature the system is subject to standard thermal activation with $\Delta V_{i \rightarrow j} \gg \Delta V_{j \rightarrow i}$ resulting in $\kappa V_{i \rightarrow j} \gg \kappa V_{j \rightarrow i}$. Effectively, this inhibits any backwards

slip yielding

$$\frac{dp_i}{dt} = -\kappa_{i \rightarrow j} p_i,$$

which make the relationship between friction, temperature and speed follow Sang et al.'s prediction [34]

$$F = F_c - \left| \beta k_B T \ln \left(\frac{v_c}{v} \right) \right|^{2/3}, \quad v_c = \frac{2f_0 \beta k_B T}{3C_{\text{eff}} \sqrt{F_c}}, \quad (2.6)$$

where F_c is the maximum friction at $T = 0$, v_c a critical velocity, f_0 is the attempt rate, C_{eff} is the effective stiffness, and β is a parameter determined by the shape of the corrugation well. Eq. (2.6) characterizes the decrease in friction with temperature in the thermal activation regime shown in Fig. 2.5a at low temperature with the assumption of only forward slips which matches well with the force traces shown in Fig. 2.5a. When the temperature is high enough that the system is consistently close to thermal equilibrium it enters the regime of thermal drift [35]. This regime transition can be understood through a comparison of two time scales: The time it takes for the moving body to travel one lattice spacing $t_v = a/v$ and the average time for a slip to occur due to thermal activation $\tau = 1/\kappa = f^{-1} \exp(\Delta V/k_B T)$. If $t_v \gg \tau$ the system falls within the thermal drift, with slips both backward and forward as shown in Fig. 2.5b, and the friction follows the prediction of Krylov et al. [35–37]

$$F \propto \frac{v}{T} e^{1/T}.$$

Should we comment about the velocity dependence being different here also?

2.4.1.2 Sliding speed

In the thermal activation regime (low temperature) and at low speeds the friction relation follow Eq. (2.6) that friction scales logarithmically with speed. For higher speed, $v > v_c$, if only thermal effects are considered, Eq. (2.6) predicts that friction will eventually saturate and come to a plateau at $F_{\text{fric}} = F_C$. This is illustrated in Fig. 2.6 with this prediction being represented by the dotted line. However, as given away by the figure, for higher speed the model will enter an athermal regime where the thermal effects are negligible compared to other contributions [31][32]. In the athermal regime the damping term muv will dominate yielding $F \propto v$. The athermal regime is often observed in reduced models if the system is overdamped or at high speeds. This concept is worth noting for later reference to MD simulations where the accessible speeds often fall into the athermal regime [38]. It is unclear how this effects real physical systems for which exist more dissipation channels than just a single viscous term [39].

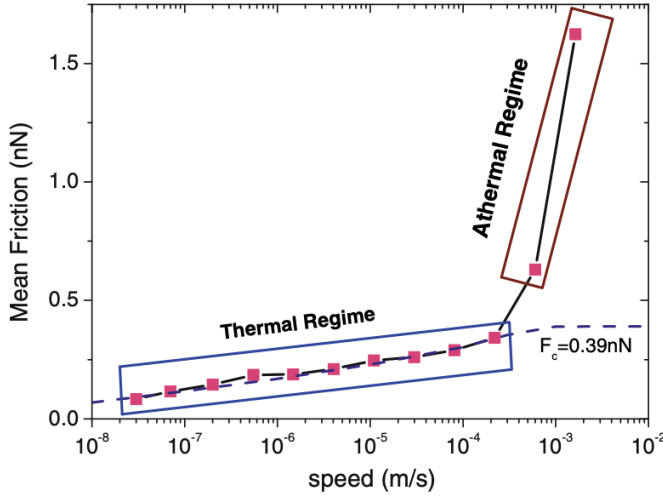


Fig. 6 Speed dependence of friction illustrating two different regimes. In the thermal regime, there is a logarithmic scaling of friction with speed, and in the athermal regime the friction is governed by the damping term such that $F \propto v$. The friction plateau ($F_c = 0.39$ nN) predicted by thermal activation is identified by the dashed line. Other model parameters: $m = 10^{-12}$ kg, $U = 0.6$ eV, $T = 300$ K, $v = 4 \times 10^3$ nm/s, $\mu = 2\sqrt{k/m}$, $a = 0.288$ nm

Figure 2.6: Temporary figure from [31]

2.4.1.3 Mass

In short the mass of the tip affects the dynamics due to the change in inertia. A smaller inertia leads to a larger attempt rate a causing an earlier (lower temp.) transition in temperature regime (to the thermal drift regime) and later speed saturation meaning a later (at larger speed) transition into the athermal regime.

2.4.1.4 Friction Regimes: Smooth Sliding, Single Slip, and Multiple Slip

Atomic friction can be divided into three regimes: smooth sliding where the tip slides smoothly on the substrate, single slip where the tip stick at one potential well and then slip to next by a jump of one lattice spacing, and multiple slip where multiple lattice spacing is jumped. Stick-slip motion is a crucial instability mechanism associated with high energy dissipation and high friction and thus controlling the transition between smooth sliding and stick-slip has been considered key to control friction. The underlying mechanism behind these regimes can be divided in static and dynamic mechanism. To understand the static mechanism we can consider a quasistatic process for which temperature, speed and damping can be neglected and where we must have $\partial(V)/\partial x = 0$ which simplifies Eq. (2.3) to

$$\frac{\pi U}{a} \sin\left(\frac{2\pi x}{a}\right) \frac{2\pi}{a} = k(vt - x), \quad (2.7)$$

with vt being the moving body position. The friction regime is determined by the number of solutions x to Eq. (2.7). One solution corresponds to smooth sliding, two solutions to a single slip and so on. It turns out that the regimes can be defined by the parameter $\eta = 2\pi^2 U/a^2 k$ yielding the first transitions at $\eta = 1, 4.6, 7.79$ and 10.95 such that $\eta \leq 1$ corresponds to smooth sliding, $1 < \eta \leq 4.6$ to a single slip and so on [40, 41]. These statics derivation lays out the foundation for the probability. Considering the dynamics on top we find that damping, speed and temperature will affect this. A high damping, high transfer of kinetic energy to heat, will result in less energy available for making multiple slips. Similar we find that increasing the speed will contribute to more kinetic energy that will increase the chances of multiple slips. Finally temperature will contribute to earlier slips due to thermal activation such that less potential energy can accumulate, and will result in fewer multiple slips. The effects of damping, speed and temperature is illustrated in Fig. 2.7

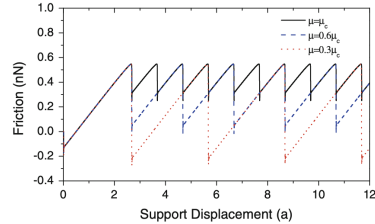


Fig. 9 The effect of damping on transitions between slip regimes where $\mu_c = 2\sqrt{k/m}$ is the critical damping coefficient. Single, double, and triple slip occur at $\mu = \mu_c$, $0.6 \mu_c$, and $0.3 \mu_c$, respectively. The abscissa has units of the lattice spacing a to facilitate identification of the transitions between single, double, and triple regimes. Other model parameters: $U = 0.6 \text{ eV}$, $T = 0 \text{ K}$, $v = 1 \mu\text{m/s}$, $m = 10^{-12} \text{ kg}$, $k = 1 \text{ N/m}$, $a = 0.288 \text{ nm}$

(a)

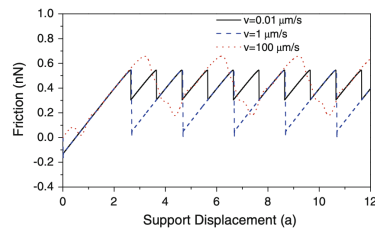


Fig. 10 The effect of sliding speed on transitions between slip regimes. Single, double, and triple slip occur at $v = 100$, 1 , and $0.01 \mu\text{m/s}$, respectively. Other model parameters: $U = 0.6 \text{ eV}$, $T = 0 \text{ K}$, $\mu = 0.8 \mu_c$, $m = 10^{-12} \text{ kg}$, $k = 1 \text{ N/m}$, $a = 0.288 \text{ nm}$

(b)

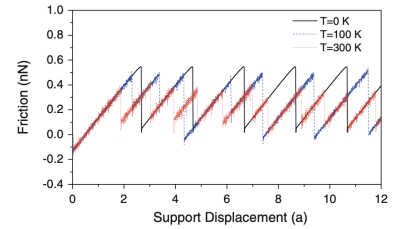


Fig. 11 The effect of temperature on transitions between slip regimes. Other model parameters: $U = 0.6 \text{ eV}$, $v = 1 \mu\text{m/s}$, $\mu = 0.6 \mu_c$, $m = 10^{-12} \text{ kg}$, $k = 1 \text{ N/m}$, $a = 0.288 \text{ nm}$

(c)

Figure 2.7: [Temporary] figure from [31]

2.4.1.5 2D nature

?

2.4.2 Frenkel-Kontorova

The standard Frenkel-Kontorova (FK) model consists of a 1D chain of N classical particles of equal mass, representing atoms, interacting via hamonic forces and moving in a sinusoidal potential as sketched in Fig. 2.8 [15]. The hamiltonian is

$$H = \sum_{i=1}^N \left[\frac{p_i^2}{2m} + \frac{1}{2}K(x_{i+1} - x_i - a_c)^2 + \frac{1}{2}U_0 \cos\left(\frac{2\pi x_i}{a_b}\right) \right], \quad (2.8)$$

where the atoms are labelled sequentially $i = 1, \dots, N$. The first term $p_i^2/2m$ represents the kinetic energy with momentum p_i and mass m . Often the effects of inertia are neglected, referred to as the static FK model, while the inclusion in Eq. (2.8) is known as the dynamic FK model [42]. The next term describes the harmonic interaction with elastic constant K , nearest neighbour distance $\Delta x = x_{i+1} - x_i$ and corresponding nearest neighbour equilibrium distance a_c . The final term represents the periodic substrate potential, serving as the external potential on site, with amplitude U_0 and period a_b . Different boundary choices can be made where both free ends and periodic conditions gives similar results. The choice of fixed ends however makes the chain incapable of sliding.

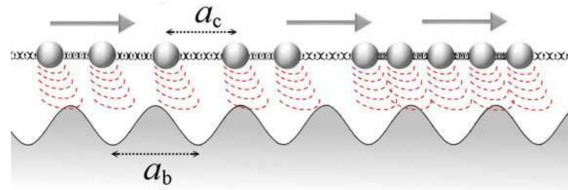


Figure 1. A sketch of the FK model, showing the two competing lengths: the average interparticle spacing and the lattice periodicity of the substrate.

Figure 2.8: [Temporary] figure from [15]

To probe static friction one can apply an external adiabatically increasing force until sliding accours. This corresponds to the static FK model, and it turns out that the sliding properties are entirely governed by its topological excitations referred to as so-called *kinks* and *antikinks*

2.4.2.1 Commensurability

We can subdivide the frictional behaviour in terms of commensurability, that is, how well the spacing of the atoms match the periodic substrate potential. We describe this by the length ratio $\theta = a_b/a_c = N/M$ where M denotes the number of minemas in the potential (within the length of the chain). A rational number for θ means that we can achieve a perfect alignment between the atoms in the chain and the potential minemas, without stretching the chain, corresponding to a *commensurate* case. If θ is irrational the chain and substrate cannot fully align without some stretching of the chain, and we denote this as being *incommensurate*.

We begin with the simplest commensurate case of $\theta = 1$ where the spacing of the atoms matches perfectly with the substrate potential periodicity, i.e. $a_c = a_b$, $N = M$. The ground state (GS) is the configuration where each atom is aligned with one of the substrate minima. By adding an extra atom to the chain we would effectively shift some of the atoms out of this ideal state, giving rise to a kink excitation. This leads to the case where two atoms will have to “share” the same potential corrugation as sketched in Fig. 2.10. On the other hand, removing an atom from the chain results in an antikink excitation where one potential corrugation will be left “atomless”. In order to reach a local minimum the kink (antikink) will expand in space over a finite length such that the chain undertakes a local compression (expansion). When applying a tangential force to the chain it is much easier for an excitation to move along the chain than it is for the non-excited atoms since the activation energy ϵ_{PN} for a kink/antikink displacement is systematically smaller (often much smaller) than the potential barrier U_0 . Thus, the motion of kinks (antikinks), i.e. the displacement of extra atoms (atom vacancies), is representing the fundamental mechanism for mass transport. These displacements are responsible for the mobility, diffusivity and conductivity within this model.

In the zero temperature commensurable case with an adiabatical increase in force, all atoms would be put into an accelerating motion as soon as the potential barrier energy is present. However, in reality any thermal excitation would excite the system before this point is reached resulting in kink-antikink pairs traveling down the chain. For a chain of finite length these often occur at the end of the chain running in opposite direction. As a kink travels down the chain the atoms are advanced by one lattice spacing a_b along the substrate potential. This cascade of kink-antikink excitations is shown in Fig. 2.9

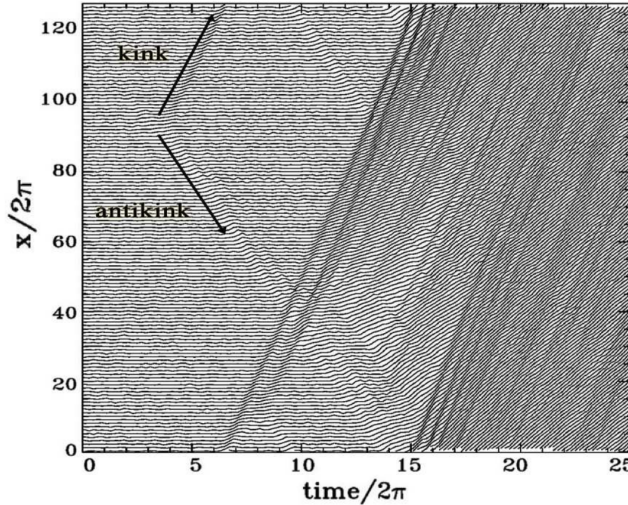


Figure 2. Time dependence of the atomic trajectories for the fully matched ($\theta = 1$) FK model at the (low-temperature) onset of depinning. Motion starts with the nucleation of a kink-antikink pair. The kink and the antikink depart in opposite directions cross the periodic boundary conditions, and collide quasielastically. A second kink-antikink pair forms in the wake of the initial kink. Further kink-antikink pairs are generated, with an avalanche-like increase of the kink-antikink concentration, eventually leading to a sliding state. Adapted from Ref. [21], Copyright (1997) by The American Physical Society.

Figure 2.9: Temporary figure from [15]

For the 2D case where an island (or flake) is deposited on a surface, in our case the graphene sheet on the Si substrate, we generally also expect the sliding to be initiated by kink-antikink pairs at the boundary.

For the case of incommensurability, i.e. $\theta = a_b/a_c$ is irrational, the GS is characterized by a sort of ‘‘staircase’’ deformation. That is, the chain will exhibit regular periods of regions where the chain is slightly compressed (expanded) to match the substrate potential, separated by kinks (antikinks), where the increased stress is eventually released as illustrated in Fig. 2.10



Figure 2.10: [Temporary] figure from url`http://www.iop.kiev.ua/ obraun/myreprints/surveyflk.pdf` p. 14. Incommensurable case ($\theta = ?$) where atoms sit slightly closer than otherwise dictated by the substrate potential for which this regularly result in a kink here seen as the presence of two atoms closely together in one of the potential corrugations.

The incommensurable FK model contains a critical elastic constant K_c , such that for $K > K_c$ the static friction F_s drops to zero, making the chain able to initiate a slide at no energy cost, while the low-velocity kinetic friction is dramatically reduced. This can be explained by the fact that the displacement occurring in the incommensurable case will yield just as many atoms climbing up a corrugation as there are atoms climbing down. For a big (infinite) chain this will exactly balance the forces making it non-resistant to sliding. Generally, incommensurability guarantees that the total energy (at $T = 0$) is independent of the relative position to the potential. However, when sliding freely a single atom will eventually occupy a maximum of the potential. When increasing the potential magnitude U_0 or softening the chain stiffness, lowering K , the possibility to occupy such a maximum disappears. This marks the so-called Aubry transition at the critical elastic constant $K = K_c(U_0, \theta)$ where the chain goes from a free sliding to a *pinned state* with a nonzero static friction. K_c is a discontinuous function of the ratio θ , due to the reliance on irrational numbers for incommensurability. The minimal value $K_c \simeq 1.0291926$ in units $[2U_0(\pi/a_b)^2]$ is achieved for the golden-mean ratio $\theta = (1 + \sqrt{5}/2)$. Notice that the pinning is provided despite translational invariance due to the inaccessibility to move past the energy barrier which act as a dynamical constraint. The Aubry transition can be investigated as a first-order phase transition for which power laws can be defined for the order parameter, but this is beyond the scope of this thesis.

The phenomena of non-pinned configurations is named *superlubricity* in tribological context. Despite the misleading name this refers to the case where the static friction is zero while the kinetic friction is nonzero but reduced. For the case of a 2D sheet it is possible to alter the commensurability, not only by changing the lattice spacing through material choice, but also by changing the orientation of the sheet relative to the substrate. Dienwiebel et al. [43] have shown that the kinetic friction, for a graphene flake sliding over a graphite surface (multiple layers of graphene), exhibits extremely low friction at certain orientations as shown in Fig. 2.11. We clearly see that friction changes as a function of orientation angles with only two spikes of considerable friction force.

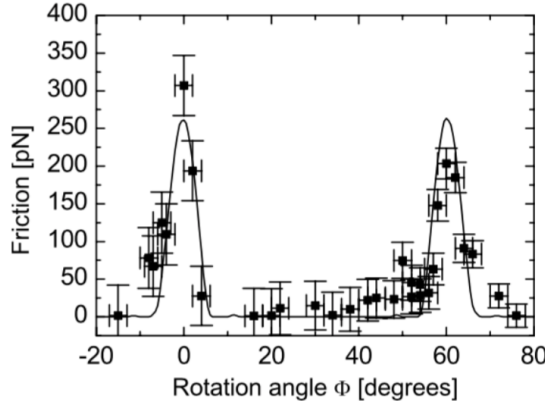


Fig. 6. Average friction force versus rotation angle Φ of the graphite sample around an axis normal to the sample surface. Two narrow peaks of high friction are observed at 0° and 61° , respectively. Between these peaks a wide angular range with ultra-low friction, close the detection limit of the instrument, is found. The first peak has a maximum friction force of 306 ± 40 pN, and the second peak has a maximum of 203 ± 20 pN. The curve through the data points shows results from a Tomlinson model for a symmetric 96-atom graphite flake sliding over the graphite surface (for details about the calculation see [39]).

Figure 2.11: [Temporary] figure from [43] showing superlubricity for incommensurable orientations between graphene and graphite. [temporary]

2.4.2.2 Kinetic friction

In the FK model the kinetic friction is primarily caused by resonance between the sliding induced vibrations and phonon modes in the chain [42]. The specific dynamics is found to be highly model and dimension specific, and even for the 1D case this is rather complex. However, we make a simplified analysis of the 1D rigid chain case to showcase the reasoning behind the phenomena.

When all atoms are sliding rigidly with center of mass velocity v_{CM} the atoms will pass the potential maxima with the so-called *washboard frequency* $\Omega = 2\pi v_{CM}/a_b$. For a weak coupling between the chain and the potential we can use the zero potential case as an approximation for which the known dispersion relation for the 1D harmonic chain is given [44, p. 92]

$$\omega_k = \sqrt{\frac{4K}{m}} \left| \sin\left(\frac{k}{2}\right) \right|,$$

where ω_k is the phonon frequency and $k = 2\pi i/N$ the wavenumber with $i \in [N/2, N/2)$. Resonance will occur when the washboard frequency Ω is close to the frequency of the phonon modes ω_q in the chain with wavenumber $q = 2\pi a_c/a_b = 2\pi\theta^{-1}$ or its harmonics nq for $n = 1, 2, 3, \dots$ [45]. Thus, we can approximate the resonance center of mass speed as

$$\begin{aligned} n\Omega &\sim \omega_{nq} \\ n\frac{2\pi v_{CM}}{a_b} &\sim \sqrt{\frac{4K}{m}} \left| \sin\left(\frac{2n\pi\theta^{-1}}{2}\right) \right| \\ v_{CM} &\sim \frac{\sin(n\pi\theta^{-1})}{n\pi} \sqrt{\frac{Ka_b^2}{m}}. \end{aligned}$$

When the chain slides with a velocity around resonance speed, the washboard frequency can excite acoustic phonons which will dissipate to other phonon modes as well. At zero temperature the energy will transform back and forth between internal degrees of freedom and center of mass movement of the chain. Hence, at zero

temperature this is in fact theorized to speed up the translational decay [42]. However, for the more realistic case of a non-zero temperature the substrate serves as a thermostat, for which energy will dissipate from the chain to the substrate degrees of freedom, giving rise to kinetic friction. This suggests that certain sliding speeds will exhibit relatively high kinetic friction while others will be subject to extremely low kinetic friction. Simulations of concentric nanotubes in relative motion (telescopic sliding) have revealed the occurrence of certain velocities at which the friction is enhanced, corresponding to the washboard frequency of the system [15]. The friction response was observed to be highly non-linear as the resonance velocities were approached.

A common way to model the non-zero temperature case is by the use of a Langevin thermostat, which models the dissipation of heat by adding a viscous damping force and thermal fluctuations by the addition of Gaussian random forces with variance proportional to the temperature (see Sec. 3.3.1 for more details). In combination, this gives rise to a kinetic friction that is both velocity and temperature dependent. By extending the FK model into 2D [42] it can be shown numerically that the friction coefficient generally increases with increasing velocity and temperature respectively, although the specific of the trend is highly sensitive to model parameters.

2.4.3 Dependence

They look at Prandtl–Tomlinson (PT) models. Is this already covered? FK?

Frictional regimes:

“Atomic friction can be divided into different regimes: smooth sliding where the AFM tip slides smoothly on the substrate, single slip where the tip sticks at one point and then jumps over one lattice spacing to another point, and multiple slip where the tip jumps over a few (more than one) lattice spacings. Stick-slip motion is a very important instability mechanism and is associated with high friction and energy dissipation. Finding ways to control transitions from smooth sliding to stick-slip has been thought to be a key to prescribing friction at the atomic scale.” [31]

Dynamic parameters [31]:

- Damping: Strong damping means high transfer of kinetic energy as heat which only allows single slip (not multiple slips, cannot jump multiple minima at once).
- Sliding speed: In increased speed can lead to multiple slips due to increased kinetic energy to transverse multiple potential energy barriers.
- Temperature: Thermal activation can trigger slip at an early stage. Higher temperature will result in less potential energy accumulated and so less kinetic energy transferred in slips

2.4.4 Experimental procedures

Experimentally, the study of nanoscale friction is challenging due to the low forces on the scale of nano-newtons along with difficulties of mapping the nano-scale topography of the sample. In opposition to numerical simulations, which provides full transparency regarding atomic-scale structures, sampling of forces, velocities and temperature, the experimental results are limited by the state-of-the-art experimental methods. In order to compare numerical and experimental results it is useful to address the most common experimental.

2.4.4.1 Scanning Probe Microscopy

Scanning probe microscopy (SPM) includes a variety of experimental methods which is used to examine surfaces with atomic resolution [46, pp. 6-27]. This was originally developed for surface topography imaging, but today it plays a crucial role in nanoscale science as it is used for probe-sampling regarding tribological, electronic, magnetic, biological and chemical character. The family of methods involving the measurement of forces is generally referred to as *scanning force microscopies* (SFM) or for friction purposes *friction force microscopes* (FFM).

One such method arose from the *atomic force microscope* AFM, which consists of a sharp micro-fabricated tip attached to a cantilever force sensor, usually with a sensitivity below 1 nN all the way down to pN. The force is measured by recording the bending of the cantilever, either as a change in electrical conduction or more commonly, by a light beam reflected from the back of the cantilever into a photodetector [1, p. 183]. By adjusting the tip-sample height to keep a constant normal force while scanning across the surface this can be used to produce a surface topography map. By tapping the material (dynamic force microscopy) with sinusoidally

vibrated tip the effects from friction and other disturbing forces can be minimized in order to produce an even clearer image (include example, preferable showing the surface structure of graphene). However, when scanning perpendicularly to the cantilever axis, one is also able to measure the frictional force as torsion of the cantilever. By having four quadrants in the photodetector (as shown in figure Fig. 2.12), one can simultaneously measure the normal force and friction force as the probes scans accross the surface.

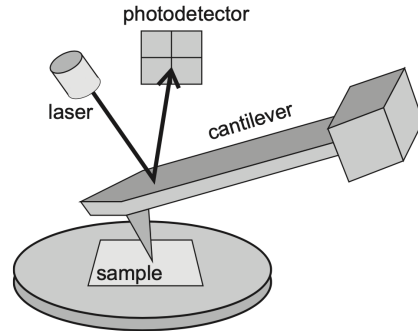


Figure 17.1 Schematic diagram of a beam-deflection atomic force microscope.

Figure 2.12: [Temporary figure from [1, p. 184]

AFM can also be used to drag a nanoflake accross the substrate as done by Dienwiebel et al. [43], where a graphene flake was attached to a FFM tip and dragged accross graphite. Notice that this makes the normal loading concentrated to a single point on the flake rather than achieving an evenly distributed load.

2.4.4.2 Surface Force Apparatus (SFA)

I think this refers to having two interfaces sliding against each other with (optionally I think) lubrication between. This is often mirrored in MD simulations and often experimental results refer to this. So it might be worth saying a few words about, but I'm not sure yet.

2.4.5 Numerical procedures

2.5 Expected frictional properties of graphene

Several studies have investigated the frictional behaviour of graphene by varying different parameters such as normal force, sliding velocity, temperature, commensurability and graphene thickness [47]. In general, we find three types of systems being studied: 1) An FFM type setup where the graphene, either resting on a substrate or suspended, is probed by an AFM tip scanning across the surface. 2) SFA approach with the graphene “sandwiched” in between two substrate layers moving relative to each other using the graphene as a solid lubricant. 3) A graphene flake sliding on a substrate, either being dragged by an AFM tip or by more complex arrangements in numerical simulations. While only the latter case matches our intended system setup, we consider all three categories due to the sparse results available. The relevant studies which we consider are listed in Table 2.1.

Table 2.1: Update multirow line span after completing the table...

System	Type	Year	Researcher	Materials	Key words
FFM	Exp.	2015 [48]	G. Paolicelli et al.	Si tip, graphene on SiO ₂ and Ni(111) substrate	Layers, load, shear strength
		2019 [49]	Zhang et al.	Monolayer graphene	Straining sheet
	Mix	2019 [50]	Vazirisereshk et al.	Graphene, MoS ₂ and Graphene/MoS ₂ heterostructure	Low friction?
		2015 [51]	Yoon et al.	Si tip, graphene on SiO ₂	Stick-slip: tip size, scan angle, layer thickness, substrate flexibility
	Num.	2016 [52]	Li et al.	Si tip, graphene on a-Si substrate	Increasing layers
SFA	Num.	2011 [53]	Wijn et al.	Graphene flakes between graphite	Rotational dynamics, superlubricity, temperature
		2012 [54]	H. J. Kim and D. E. Kim.	Carbon sheet	Corrugated nano-structured surfaces
Flake	Exp	2005 [43]	Dienwiebel et al.	Graphene on graphite	Commensurability, superlubricity
		2013 [55]	Feng et al.	Graphene on graphite	Free sliding (relevant?)
	Num.	2009 [56]	Bonelli et al.	Graphene on graphite	Tight-binding, commensurability, load, flake size
		2012 [57]	Reguzzoni et al.	Graphene on graphite	Graphite thickness
		2014 [58]	Liu et al.	Graphene on graphite	Thickness, deformations, high speed
		2018 [59]	P. Zhu and Li	Graphene on gold	Flake size, commensurability
		2019 [60]	Zhang et al.	Graphene on diamond	Temperature, sliding angle, friction coefficient

One of the earliest tribological simulations of graphene was carried out by Bonelli et al. [56] in 2009 using a tight-binding method (excluding thermal excitations) to simulate a graphene flake on an infinite graphene sheet [47]. They implemented a FKT-like setup where each atom in the flake is coupled horizontally to a rigid support by elastic springs. They recovered the stick-slip behaviour, which is also observed in FFM setups both experimentally [49] and numerically [52][59], and they found an agreement with the qualitative observation that soft springs allow for a clean stick-slip motion while hard springs inhibit it ($\lesssim 40$ N/m). In AFM and SFA experiments, the stick-slip motion tends to transition into smooth sliding when the speed exceeds $\sim 1\mu\text{s}$ while in MD modelling the same transition is observed in the $\sim 1\text{ m/s}$ region [15]. This 6 order of magnitude discrepancy has been largely discussed in connection to simplifying assumptions in MD simulations.

Bonelli et al. [56] also found that commensurability, through orientation of the flake and the direction of sliding, to be of high importance for the frictional behaviour which generally aligns with the predictions of the FK type models. They confirmed qualitatively the experimental observation of superlubricity for certain incommensurable orientations as shown experimentally by Dienwiebel et al.[43] and further supported by experimental measurements of interaction energies by Feng et al. [55]. This commensurability importance is also reported for MD simulations [60][59][53]. Bonelli et al. [56] found the friction force and coefficient to be one order of magnitude higher than that of the experimental results which they attribute to the details of the numerical modelling. Generally the experimental coefficients between graphite and most materials lies in the range 0.08-0.18 [43] and while Dienwiebel et al. [43] reported a wide range of frictional forces all the way from 28 ± 16 pN to 453 ± 16 pN in a load range $\sim [-10, 20]\text{nN}$ the change in friction with applied load was as low as 0.05-0.4 % (coef. of 0.0005-0.004). This indicates an almost independent relationship between friction and load which is attributed to the lack of change in contact area.

Furthermore, Bonelli et al. [56] found friction to decrease with flake size which is mainly attributed to the idea that boundary atoms are dominant in increasing friction, but also due to their system setup decreasing the rotational freedom as size increases. However, the decreasing friction with increasing flake size is also found for the graphene on gold MD simulation [59]. This can however be attributed to commensurability as a numerical MD study of monolayer islands of krypton on copper by Reguzzoni and Righi [61] reports that the effective commensurability increase drastically below a critical flake radius on the order of 10 Å. In a numerical study by Varini et al. [62], based on Kr islands adsorbed on Pb(111), this is further elaborated as they found that finite size effects are especially important for static friction as a pinning barrier rise from the edge (preventing otherwise superlubricity due to incommensurability). They reported a relationship $F_s \sim A^{\gamma_s}$ not only sublinear $\gamma_s < 1$ but also sublinear with respect to the island perimeter $P \propto A^{1/2}$ by having $\gamma_s = 0.25$ for a hexagonal edge and $\gamma_s = 0.37$ when circular, indicating that only a subset of the edge is responsible for the pinning effect. This aligns with the general change in friction found by [59] for different flake geometries (square, triangle, circle). Additionally, Varini et al. also found the edge pinning effect to decrease with increasing temperature as the edge energy barriers are reduced. In general this aligns with the FK models prediction of a reduction of friction due to thermal activation of the atoms overcoming the energy barriers which is also in agreement with the numerical study by Wijn et al. [53].

Evolution effects, or so-called friction strengthening, is also observed experimentally by Zhang et al. [49] (only when on substrate) and numerically by Li et al. [52], meaning that the friction force increase during the initial stick-slip cycles. However, this is only found when having the graphene sheet resting on a substrate [49] opposed to a suspended sheet, and it was found to diminish when increasing the number of graphene layers stacked (graphite) [52]. In general the friction was found to decrease with increasing number of layers which is also supported by the findings in [51] but disagree with [57]?? Zhang et al. [49] additionally found that straining a suspended stretch, modulating the flexibility which consequently change the local pinning capability of the contact interface and lowers the dynamic friction. Another surface manipulating study was performed by H. J. Kim and D. E. Kim. [54] where the investigated the effects of corrugated nano-structured surfaces which altered the contact area and structural stiffness resulting in both increased and slightly decreased friction under certain load ranges.

Negative friction coefficients **TO-DO**.

The main qualitative expectations regarding our system are summarized in ??

Table 2.2: Qualitative trends

Stick slip	Generally we expect to observe periodic stick-slip motion with a period matching the lattice constant(s) involved [18]. This is however inhibited for high stiffness of the spring coupling to a driving support and at large sliding velocity.
Static friction	The static friction is highly related to the presence of stick-slip motion. The static friction is most pronounced for commensurable configurations and will decrease drastically for incommensurability. However, further reduction of static friction is expected for an increasing flake size and increasing temperature.
Commensurability	Both static and dynamic friction is expected to be highly sensitive to commensurability, through lattice spacing, orientation of the flake relative to the substrate and by the path of sliding along the substrate. By changing the spring stiffness of the coupled driving support we expect to get a response in commensurability due to a change in translational freedom.
Friction evolution (Friction strengthening)	Friction evolution is found to be present in mono layer graphene resting on a substrate, and thus we expect this to be present in our simulation setup as well.
Negative coef	TO-DO

Having considered some qualitative expectations we take a look at the quantitative expectations for the variables such as load, velocity, temperature and contact area.

The dependency on friction of normal load turns out to be a complex matter and has proven to be highly system dependent. As already mentioned, asperity theory mainly point to a sublinear relationship between friction and load, while the FK models gives no direct predictions other than this affect the energy barriers and thus phonon dissipation. Experimentally rather different trends have been observed, although the majority agree on increasing friction with increasing load [1, p. 200]. For the graphene flake Dienwiebel et al. [43] found a seemingly non-dependent relationship while, FFM study by G. Paolicelli et al. [48] found a great fit with the sublinear predictions of Maugis-Dugdale theory ($F_f \propto (F_N - F_{N,0})^{2/3}$). Here the discrepancy might lie in the difference between a spherical tip indenting the graphene sheet (matching asperity theory) as opposed to two flat graphene/graphite sheets in contact (matching FK models). However, numerical studies with graphene in contact with graphite still find both sublinear [56] and linear [60] load dependencies.

Generally a increasing logarithmic velocity dependence is found in experimental AFM studies [1, p. 201] associated to thermally activated hopping of the scanning tip. At higher velocities thermally activated processes are less important and friction becomes independent of velocity. This has been observed for Si tips and diamond, graphite and amorphous carbon surfaces with scan velocities above $1\text{ }\mu\text{/s}$. Guerra et al. [63] have studied gold clusters on graphite using MD simulations. They found a viscous friction, friction is proportional to sliding velocity, response in both low and high speed domains. However, thermal effects reversed: at low speed (diffusive) friction decreased with increased temperature while at high speed (ballistic) speed friction increases with temperature. In the MD simulations the crossover from ballistic to diffusive occur between 10 and 1 m/s.

Experimentally Zhao et al. observed in a series of AFM on MATERIAL that friction decreases strongly with temperature as $F_{\text{fric}} \propto \exp(1/T)$. This matches theoretical predictions by Krylov et al. [35] which attributes this to thermal activation inhibiting stick-slip behaviour.

Wijn et al. [53] find that friction commensurability can be lost at higher temperature (above 200K) were the found a power law behaviour $F_k \propto T^{-1.13 \pm 0.04}$.

Zhang et al. [60] found that friction increased with temperature, using a velocity of 10 m/s. Considering the findings of [63] this discrepancy might be due to low speed diffusive behaviour as opposed to high speed ballistic behaviour.

Table 2.3: Qualitative trends

Normal load	Generally an increasing friction force is expected with increasing load. Both non-dependent, sublinear and linear relationship can be expected here.
Velocity	Generally an increasing friction force is expected with increased sliding velocity. Experimental results suggest that kinetic friction goes as $F_k \propto \ln(v)$, with the expectation that friction become independent of velocity at ‘high’ velocities above $1\text{ }\mu\text{/s}$. Numerically a viscous $F_k \propto v$ is expected for all velocity ranges.
Temperature	.

Table 2.4: Quantitative nano friction dependence on various variables. work in progress.

Variable	Dependency	Numerical studies	Experimental
Normal force F_N	$F_{\text{fric}} \propto F_N^\alpha$ $\alpha \leq 1$	Zhang et al. [60] finds a seemingly linear relationship $F_{\text{fric}} \propto F_N$ while Bonelli et al. [56] reports a sublinear relationship. The latter corresponds with that of nanosasperity simulations where Mo et al. [18], using an amorphous carbon tip on a diamond sample, also found a sublinear relationship when including adhesion and linear without adhesion.	Experimentally rather different trends have been observed, although the majority agree on increasing friction with increasing load [1, p. 200]. For the graphebne flake Dienwiebel et al. [43] found a seemingly non-dependent relationship while Feng et al. [55] did not report on this. FFM analog to the single asperity setup have yielded both linear relationship [17] (silicon tip on gold) while Schwarz et al. [64] found that FFM with well-defined spherical tips matched with theoretical results (DMT, elastic spheres pressed together [1, p. 200]), yielding a power law $F_{\text{fric}} = F_N^{2/3}$.
Velocity v	$F_{\text{fric}} \propto \ln v$ (exp.) or $F_{\text{fric}} \propto v$ (num.)	Studies of gold clusters on graphite suggest that friction is viscous, i.e. proportional to velocity [15].	Logaritmic velocity dependence of friction has been measured for nanotip friction [1, p. 201] associated to thermal activation and possibly the time available to form bond between the tip and the substrate. At higher velocities thermally activated processes are less important and friction becomes independent of velocity. This has been observed for Si tips and diamond, graphite and amorphous carbon surfaces with scan velocities above $1 \mu\text{s}$.
Temperature T	Either increase (MD) or decrease as $F_{\text{fric}} \propto \exp(1/T)$ (experimental)	Zhang et al. [60] found simply that friction increased with temperature. The [15] gold cluster on graphite study (get reference) found that the temperature dependence was dependent on velocity regime. Low speed (diffusive) friction decreases upon heating while high speed (ballistic) friction rises with temperature.	Zhao et al. [65] found $F_{\text{fric}} \propto \exp(1/T)$.
Real contact area A	$F_{\text{fric}} \propto A$	Mo et al. [18] found that $F_{\text{fric}} \propto A$ where A is the real contact area defined by atoms within chemical range. This is not studied for the case of a nanoflake where the contact area is presumably rather constant.	

2.6 Research questions

Chapter 3

Molecular Dynamics

Thanks to advances in computing algorithms and hardware the recent years has witnessed a remarkable increase in our ability to simulate tribological processes in realistic nano-frictional system [15]. A Molecular dynamics (MD) simulation can be considered as computational “experiment”. Given a set of initial conditions and a mathematically model for interatomic forces we can solve Newton’s (or equivalent) equation of motion by numerical integration [p. 303]BHUSHAN20051507. The interatomic forces are derived from interparticle interaction potentials, which is the heart of MD simulations and the specific choice of potentials can often be quite challenging.

Alternatives to the MD simulation like Ab initio methods calculate the interaction based on quantum mechanics (solving schrödinger) right?

3.1 Potentials

The potentials used in our MD simulation is mainly based on the of Li et al. [52] which have a somewhat similar MD friction simulation setup. Li et al. impose a Silicon tip on the graphene sheet supported by a Silicon substrate where we slide the whole sheet upon the substrate. Nonetheless, this serves as a good anchor for the methodology of the setup. The covalent bonds of C-C in graphene and Si-Si in the substrate is described by the Tersoff and Stillinger–Weber potentials, respectively. A typical 12-6 Lennard–Jones potential is used to describe the van der Waals adhesive interaction between graphene and the substrate.

3.1.1 General formulation of potentials (?)

On a general note we can generalize the n-body potential as the expansion in orders of participating atoms as

$$E = \sum_i V_1(\mathbf{r}_i) + \sum_{i,j} V_2(\mathbf{r}_i, \mathbf{r}_j) + \sum_{i,j,k} V_3(\mathbf{r}_i, \mathbf{r}_j, \mathbf{r}_k) + \dots,$$

where \mathbf{r}_n is the position of the n th particle and V_m is called an m -body potential [66]. The first one-body term corresponds to an external potential, followed by the two-body term, the three-body term and so on. The simplest model that includes particle interaction is the pair potential truncating the expansion after the two-body term. A general feature of the pair potentials is that they favor close-packed structures which is unsuited to describe covalent bonds that take more open structures. In particular, pair potentials are completely inapplicable to strongly covalent systems [66]. In order to accomodate the description of covalent bonds the natural step is thus to include the next step of the expansion, the three-body terms, as we will see for the modeling of the C-C bonds in the graphene sheet and the Si-Si bonds in Silicon substrate. For the interaction between the sheet and the substrate we use a Lennard Jones pair potential describing the non-bonded van der Waals interaction. This simple interaction model between the moving object and substrate has come to be the standard in friction simulations [59], [67], [51], [3].

3.1.2 Lennard Jones

TODO: Add potential curve figure

This sections is based on [68], [69], [70].

The Lennard-Jones (LJ) model is probably one of the most famous pair potentials used in MD simulations. LJ models the potential energy between two non-bonding atoms solely based on interatomic distance. The model accounts for attractive forces arising from dipole-dipole, dipole-induced dipole and London interactions, and repulsive forces that capture the hard core of overlapping wave functions at small distances (**double check this statement**). Thus, it assumes neutrally charged atoms and was originally proposed for noble gases. The classical 12-6 version of the model (referring to the power law of the repulsive and attractive forces respectively) reads

$$E = 4\epsilon \left[\left(\frac{\sigma}{r} \right)^{12} - \left(\frac{\sigma}{r} \right)^6 \right], \quad r < r_c, \quad (3.1)$$

where r is the interatomic distance with cut-off r_c , ϵ is the depth of the potential well and σ the interatomic distance where the potential is zero. By solving for the potential minimum ($dE/dr = 0$) we find the equilibrium distance to be $r_0 = \sigma 2^{1/6}$. This makes for a slightly more intuitive interpretation of σ which effectively sets the equilibrium distance between atoms, i.e. the dividing line for which the force is repulsive or attractive.

3.1.3 Stillinger weber

TODO: Add potential figure and or figure illustrating three body angles.

This section is based on [[71], [72]]

The stillinger weber potential takes the form of a three body potential

$$E = \sum_i \sum_{j>i} \phi_2(r_{ij}) + \sum_i \sum_{j \neq i} \sum_{k>j} \phi_3(r_{ij}, r_{ik}, \theta_{ijk}),$$

where r_{ij} denotes the distance between atom i and j and θ_{ijk} the angle between bond ij and jk . The summations is over all neighbours j and k of atom i within a cut-off distance $r = a\sigma$.

The two-body term ϕ_2 builds from the LJ model with the addition of an exponential cutoff term

$$\phi_2(r_{ij}) = A_{ij} \epsilon_{ij} \left[B_{ij} \left(\frac{\sigma_{ij}}{r_{ij}} \right)^{p_{ij}} - \left(\frac{\sigma_{ij}}{r_{ij}} \right)^{q_{ij}} \right] \exp\left(\frac{\sigma_{ij}}{r_{ij} - a_{ij}\sigma_{ij}}\right). \quad (3.2)$$

The model parameters A , ϵ , B , σ , p , q and a comes with i, j indices to indicate that these parameters should be specified for each unique pair of atom types. However, in our case we will only provide a single value for each model parameter as we are exclusively dealing with Si-Si bonds. We see that the first term in Eq. (3.2) is reminiscent of the LJ model in Eq. (3.1) while the last term effectively drives the potential to zero at $r = a\sigma$, which is thus the chosen cut-off distance for the potential evaluation. With the model parameters for the Si-Si modelling (see Table 3.1) the cut-off becomes ~ 3.8 Å.

The three body term includes an angle dependency as

$$\phi_3(r_{ij}, r_{ik}, \theta_{ijk}) = \lambda_{ijk} \epsilon_{ijk} \left[\cos \theta_{ijk} - \cos \theta_{0,ijk} \right]^2 \exp\left(\frac{\gamma_{ij}\sigma_{ij}}{r_{ij} - a_{ij}\sigma_{ij}}\right) \exp\left(\frac{\gamma_{ik}\sigma_{ik}}{r_{ik} - a_{ik}\sigma_{ik}}\right), \quad (3.3)$$

where $\theta_{0,ijk}$ is the equilibrium angle. The first term of Eq. (3.3) includes an angle dependency analog to a harmonic oscillator based on a cosine angle distance from the equilibrium angle. The final two terms act again as a cut-off function by driving the potential to zero at $r_{ij} = a_{ij}\sigma_{ij}$ and $r_{ik} = a_{ik}\sigma_{ik}$ respectively.

The parameters used for the Si-Si bond modeling is displayed in Table 3.1 along with an interpretation of each model parameter.

Table 3.1: Parameters for the stilliner weber potential used for intermolecular interactions in the silicon substrate.

Parameter	Value	Description
ϵ	2.1683	Individual depth of the potential well for each atom type pair/tiplets.
σ	2.0951	Distance for which the individual pair interactions has zero potential (analog to the LJ model).
a	1.80	The individual cut-off distance for each atom type pair.
λ	21.0	The overall depth of the three-body potential well.
γ	1.20	The shape of the three-body cut-off terms.
$\cos(\theta_0)$	-1/3	Cosine of equilibrium angle.
A	7.049556277	The overall depth of the two-body potential well.
B	0.6022245584	Scales the repulsion part of the two-body term.
p	4.0	The power dependency for the repulsion part of the two-body term.
q	0.0	The power dependency for the attraction part of the two-body term.
tol	0.0	LAMMPS: Option to define a different cut-off than the theoretical of $r = a\sigma$. $tol = 0$ refers to the theoretical being used.

3.1.4 Tersoff

This section is based on [[73], [66]].

The tersoff potential abandon the idea of a general n -body form and attempts instead to build the model on a more physics informed approach; The more neighbours an atom has the weaker the bonds will be. Thus it introduces the bond order (bond strength), that is environment specific and decrease with increasing bond coordination (number of neighbours for a given atom). The potential energy is taken to have the form

$$E = \sum_i E_i = \frac{1}{2} \sum_{i \neq j} V_{ij},$$

$$V_{ij} = f_C(r_{ij}) [f_R(r_{ij}) + b_{ij} f_A(r_{ij})],$$

where the total potential energy is decomposed into a bond energy V_{ij} . The indices i and j run over the atoms of the system with r_{ij} denoting the distance between atom i and j . Notice that the sum includes all combinations of i, j where $i \neq j$ meaning that the same bond is double counted which is the reason for the additional factor 1/2. The reasoning behind comes from the asymmetry of the bond order $b_{ij} \neq b_{ji}$ leading to a $V_{ij} \neq V_{ji}$. The bond energy is composed of a repulsive term f_R , arising from overlapping wave functions, and an attractive term f_A associated with bonding. f_C is simply a smooth cut-off function to increase computational efficiency. b_{ij} represent the bond order, i.e. the strength of the bonds, which depends inversely on the number of bonds, the bond angles (θ_{ijk}) and optionally the relative bonds lengths (r_{ij}, r_{jk}). Notice that an additional cut-off term a_{ij} was originally multiplied to f_R as a way of including terms that limit the range of the interactions to the first neighbour shell. These kind of limitations is already included in b_{ij} for the attractive term f_A but is often omitted for the repulsive term f_R , and we do so to by setting $a_{ij} = 1$.

The cut-off function f_C goes from 1 to 0 over a small interval range $R \pm D$ as

$$f_C(r) = \begin{cases} 1 & r < R - D \\ \frac{1}{2} - \frac{1}{2} \sin\left(\frac{\pi}{2} \frac{r-R}{D}\right) & R - D < r < R + D \\ 0 & r > R + D \end{cases}$$

which is continuous and differentiable for all r . R is usually chosen to include only the first neighbour shell. The repulsive and attractive terms f_R and f_A is modelled as an exponential function, similar to a morse potential,

$$f_R(r) = A \exp(-\lambda_1 r),$$

$$f_A(r) = -B \exp(-\lambda_2 r).$$

The novel feature of the model lies in modeling of the bond order b_{ij} which includes three-body interactions by summing over a third atom $k \neq i, j$ within the cut-off $r_{ik} < R + D$ as shown in the following.

$$b_{ij} = (1 + \beta^n \zeta_{ij}^n)^{-\frac{1}{2n}} \quad (3.4)$$

$$\zeta_{ij} = \sum_{k \neq i, j} f_C(r_{ik}) g(\theta_{ijk}(r_{ij}, r_{ik})) \exp(\lambda_3^m (r_{ij} - r_{ik})^m) \quad (3.5)$$

$$g(\theta) = \gamma_{ijk} \left(1 + \frac{c^2}{d^2} - \frac{c^2}{[d^2 + (\cos \theta - \cos \theta_0)^2]} \right). \quad (3.6)$$

In Eq. (3.6) $\zeta_{i,j}$ is an effective coordination and $g(\theta)$ captures angle dependency as it is minimized at the equilibrium angle $\theta = \theta_0$.

The parameters used to model the graphene C-C bonds is summarized in Table 3.2

Table 3.2: Parameters for the tersoff potential used for intermolecular interations in the graphene sheet

Parameter	Value	Description
m	3.0	Default (not used since $\lambda_3 = 0$)
γ	1.0	...
λ_3	0.0 \AA^{-1}	...
c	3.8049×10^4	Strength of the angular effect
d	4.3484	Determines the “sharpness” of the angular dependency
$\cos(\theta_0)$	-0.57058	Cosine of the equilibrium angle
n	0.72751	Power law exponent for the bond order dependency
β	1.5724×10^{-7}	...
λ_2	2.2119 \AA^{-1}	Decay of repulsion potential term
B	346.74 eV	Attractive potential term minimum at core ($r_{ij} = 0$).
R	1.95 Å	Center distance for cut-off
D	0.15 Å	Thickness of cut-off layers
λ_1	3.4879 \AA^{-1}	Decay of repulsion potential term
A	1393.6 eV	Repulsion potential term at core ($r_{ij} = 0$)

3.2 Integration

Having defined a system of particles governed by interatomic potentials we need to move the system forward in time. By solving Newtons equations of motion we effectively sample the microcanonical ensemble characterized by a constant number of particles N , volume V and energy E , hence denoted NVE. Newtons equaitons of motion read

$$m_i \frac{d^2 \mathbf{r}_i}{dt^2} = \mathbf{F}_i = -\nabla U_i \quad (3.7)$$

where i is the particle index and m_i its mass, $\mathbf{r}_i = (x_i, y_i, z_i)$ the position, t is time, $\nabla_i = (\frac{\partial}{\partial x_i}, \frac{\partial}{\partial y_i}, \frac{\partial}{\partial z_i})$ and U_i the potential energy. The potential energy is a function of the particle positions of nearby particles depending on the specefic potential in use. Since the forces defined by the potentials is conservative we expect the energy of the solution to be conserved. We can redefine Eq. (3.7) in terms of two coupled first order differential equations

$$\dot{\mathbf{v}}_i(t) = \frac{\mathbf{F}}{m_i}, \quad \dot{\mathbf{r}}_i(t) = \mathbf{v}_i(t), \quad (3.8)$$

where $\dot{x} = dx/dt$ (Newton's notation) and $\mathbf{v} = (v_x, v_y, v_z)$ is velocity. Numerically we can solve the coupled equations by integrating over discrete timesteps. That is, we discretize the solution into temporal steps $t_k = t_0 + k\Delta t$ with start time t_0 and time-step Δt .

3.2.1 Velocity Verlet

A common algorithm to integrate Newton's equation of motion (as formulated in Eq. (3.8)) is the *velocity verlet*. We can derive the algorithm by the use of Taylor expansions. We begin by expanding the next-step position vector $\mathbf{r}_i(t + \Delta t)$ at time t

$$\mathbf{r}_i(t + \Delta t) = \mathbf{r}_i(t) + \dot{\mathbf{r}}_i(t)\Delta t + \frac{\ddot{\mathbf{r}}_i(t)}{2}\Delta t^2 + \mathcal{O}(\Delta t^3), \quad (3.9)$$

where $\ddot{\mathbf{r}} = d^2\mathbf{r}/dt^2$ and Δt^n is simply the relaxed notation for $(\Delta t)^n$. Similar we take the expansions of the next-step velocity vector $\mathbf{v}_i(t + \Delta t)$ at time t

$$\mathbf{v}_i(t + \Delta t) = \mathbf{v}_i(t) + \dot{\mathbf{v}}_i(t)\Delta t + \frac{\ddot{\mathbf{v}}_i(t)}{2}\Delta t^2 + \mathcal{O}(\Delta t^3). \quad (3.10)$$

Finally, by taking the expansion of $\dot{\mathbf{v}}_i(t + \Delta t)$ we can eliminate the $\ddot{\mathbf{v}}_i$ -term in Eq. (3.10) and simplify it as shown in the following.

$$\begin{aligned} \dot{\mathbf{v}}_i(t + \Delta t) &= \dot{\mathbf{v}}_i(t) + \ddot{\mathbf{v}}_i(t)\Delta t + \mathcal{O}(\Delta t^2) \\ \frac{\ddot{\mathbf{v}}_i(t)}{2}\Delta t^2 &= \frac{\Delta t}{2}(\dot{\mathbf{v}}(t + \Delta t) - \dot{\mathbf{v}}_i(t)) + \mathcal{O}(\Delta t^3) \\ &\Downarrow \\ \mathbf{v}_i(t + \Delta t) &= \mathbf{v}_i(t) + \dot{\mathbf{v}}_i(t)\Delta t + \frac{\Delta t}{2}(\dot{\mathbf{v}}_i(t + \Delta t) - \dot{\mathbf{v}}_i(t)) + \mathcal{O}(\Delta t^3) \\ &= \mathbf{v}_i(t) + \frac{\Delta t}{2}(\dot{\mathbf{v}}_i(t) + \dot{\mathbf{v}}_i(t + \Delta t)) + \mathcal{O}(\Delta t^3). \end{aligned} \quad (3.11)$$

By combining Eq. (3.9) and Eq. (3.11) and using Newton's second equation $\dot{\mathbf{v}} = \mathbf{F}_i(t)/m_i$ and $\mathbf{v} = \dot{\mathbf{r}}$ we arrive at the final scheme

$$\begin{aligned} \mathbf{r}_i(t + \Delta t) &= \mathbf{r}_i(t) + \mathbf{v}_i(t)\Delta t + \frac{\mathbf{F}_i(t)}{2m_i}\Delta t^2 + \mathcal{O}(\Delta t^3), \\ \mathbf{v}_i(t + \Delta t) &= \mathbf{v}_i(t) + \frac{\mathbf{F}_i(t) + \mathbf{F}_i(t + \Delta t)}{2m_i}\Delta t + \mathcal{O}(\Delta t^3). \end{aligned}$$

The scheme will give a local error of order Δt^3 corresponding to a global error of Δt^2 . One of the most popular ways to implement this numerically is as stated in the following steps.

1. Calculate $v_{k+\frac{1}{2}} = v_k + \frac{F_k}{2m}\Delta t$.
2. Calculate $r_{k+1} = r_k + v_{k+\frac{1}{2}}\Delta t$.
3. Evaluate the force $F_{k+1} = F(r_{k+1})$.
4. Calculate $v_{k+1} = v_{k+\frac{1}{2}} + \frac{F_{k+1}}{2m}\Delta t$

3.3 Thermostats

As we already mentioned above in Sec. 2, any kind of sliding friction involves mechanical work, some of which is then transformed into heat (the rest going into structural transformations, wear, etc.). The heat is then transported away by phonons (and electrons in the case of metallic sliders) and eventually dissipated to the environment [15].

Likewise all excitations generated in the simulations should be allowed to propagate in the system and disperse in the bulk of both sheet and substrate. Due to small simulation size these is likely to reflect back

and ‘‘pile up’’ unphysically. Thus in order to avoid continuous heating and attain a steady state the (Joule) heat must be removed at a steady state. This is very the viscous damping of the Langevin equations enter the picture. It can be difficult to set the value γ for the magnitude of this damping. The unphysical introduction of heat sink can be mitigated by some modifications he mention, which is kind of next level I guess.

3.3.1 Langevin thermostat

In order to control the temperature of the system we introduce the so-called Langevin thermostat. This is a stochastic thermostat that modifies Newton's equation of motion such that solution lies in the canonical ensemble characterized by a constant number of particles N , constant volume V and constant temperature T , hence denoted NVT. The canonical ensemble system is represented by the finite system being in contact with an infinite heat bath of temperature T . The NVT ensemble is equivalent to sampling a system in thermodynamic equilibrium where the weight of each microscopic state is given by the Boltzmann factor $\exp[-E/(k_B T)]$.

The Langevin equation is the modified version of Newton's second law for a Brownian particle. A Brownian particle is a small particle suspended in liquid, e.g. pollen or dust, named after Robert Brown (1773–1858) who was the first to observe its jittery motion. The Langevin equation describes this motion as the combination of viscous drag force $-\gamma \mathbf{v}$, where γ is a positive friction coefficient and \mathbf{v} the velocity vector, and a random fluctuation force \mathbf{R} . The Langevin equation reads

$$m \frac{d\mathbf{v}}{dt} = -\gamma \mathbf{v} + \mathbf{R} \quad (3.12)$$

where m is the particle mass. This effectively describes the particle of interest, the Brownian particle, as being suspended in a sea of smaller particles. The collision with these smaller particles is modelled by the drag force and the fluctuation force. We notice that if the fluctuation force is excluded Eq. (3.12) becomes

$$m \frac{d\mathbf{v}}{dt} = -\gamma \mathbf{v} \Rightarrow \mathbf{v}_i(t) = v(0) e^{-\frac{\gamma t}{m}},$$

where the solution shows that the Brownian particle will come to a complete stop after a long time $\mathbf{v}_i(t \rightarrow \infty) \rightarrow \mathbf{0}$. This is in violation with the equipartition theorem

$$\frac{1}{2} m \langle v^2 \rangle_{eq} = \frac{k_B T}{2},$$

and hence the fluctuation force is necessary to obtain the correct equilibrium.

The following calculations are done in one dimension in order to simplify the notation. We describe the statistical nature of the collisions as a sum of independent momentum transfers

$$\Delta P = \sum_i^N \delta p_i$$

where ΔP denotes the change of momentum after N momentum transfers δp_i from the environment to the Brownian particle. We assume the first and second moments $\langle \delta p \rangle = 0$ and $\langle \delta p^2 \rangle = \sigma^2$. When N is large the central limit theorem states that the random variable ΔP has a Gaussian distribution with $\langle P \rangle = 0$ and $\langle \Delta P^2 \rangle = N\sigma^2$. If we consider the momentum change ΔP over a discrete time Δt , where the number of collisions is proportional to time $N \propto \Delta t$, the corresponding fluctuation force $R = \Delta P / \Delta t$ will have a variance

$$\langle R^2 \rangle = \frac{\langle \Delta P^2 \rangle}{\Delta t^2} = \frac{N\sigma^2}{\Delta t^2} \propto \frac{1}{\Delta t}.$$

In a computer simulation we need to pick a random force $R(t)$ from a Gaussian distribution every time-step Δt . These forces will not be correlated as long as Δt is larger than the correlation time of the forces from the molecules which we will assume for this model (I think there exist corrections for this to refer to here). With this assumption we can write the correlation function as

$$\langle R(t) R(0) \rangle = \begin{cases} \frac{a}{\Delta t}, & |\Delta t| < \Delta t/2 \\ 0, & |\Delta t| > \Delta t/2, \end{cases} \quad (3.13)$$

where a is some strength of (...?). In the limit $\Delta t \rightarrow 0$ the correlation function becomes

$$\langle R(t)R(0) \rangle = a\delta(t), \quad (3.14)$$

where δ denotes the dirac delta function. This is valid for all spatial coordinates which will all be independent of each other. Since both the drag force and the fluctuation force originate from the molecular fluid, where the drag force $-\alpha v$ is velocity dependent it is reasonable to assume that fluctuation force is independent of velocity, i.e. $\langle R_i v_j \rangle = 0$ for all cartesian indices i and j .

In the following we will attempt justify the Langevin equaiton (why it is like it is) and determine the relationship between the drag coefficient γ and the random force R .

From the Langevin equation Eq. (3.12) we can compute the velocity autocorrelation function (Move to appendix?). We do this in one dimension for simplicity. We begin by multiplying by $(e^{\gamma t/m})/m$

$$\dot{v}(t)e^{\gamma t/m} + \frac{\gamma}{m}v(t)e^{\frac{\gamma t}{m}} = \frac{F}{m}e^{\frac{\gamma t}{m}},$$

and integrate from $t = -\infty$. By the use of integration by parts on the latter term on the left hand side we calculate the velocity

$$\begin{aligned} \int_{-\infty}^t dt' \dot{v}(t')e^{\frac{\gamma t'}{m}} + \frac{\gamma}{m}v(t)e^{\frac{\gamma t}{m}} &= \int_{-\infty}^t dt' e^{\frac{\gamma t'}{m}} \frac{F(t')}{m} \\ \int_{-\infty}^t dt' \dot{v}(t')e^{\frac{\gamma t'}{m}} + \left(\left[v(t')e^{\frac{\gamma t'}{m}} \right]_{-\infty}^t - \int_{-\infty}^t dt' \dot{v}(t')e^{\frac{\gamma t'}{m}} \right) &= \int_{-\infty}^t dt' e^{\frac{\gamma t'}{m}} \frac{F(t')}{m} \\ v(t) &= \int_{-\infty}^t dt' e^{\frac{-\gamma(t-t')}{m}} \frac{F(t')}{m}, \end{aligned}$$

where $e^{\frac{-\gamma t}{m}}$ plays the role of a response function. We can then calculate the autocorrelation

$$\begin{aligned} \langle v(t)v(0) \rangle &= \int_{-\infty}^t dt_1 \int_{-\infty}^0 dt_2 e^{\frac{t-t_1-t_2}{m}} \frac{\langle F(t_1)F(t_2) \rangle}{m^2} \\ &= \int_{-\infty}^t dt_1 \int_{-\infty}^0 dt_2 e^{\frac{t-t_1-t_2}{m}} \frac{a\delta(t_1-t_2)}{m^2} \\ &= \int_{-\infty}^0 dt_2 e^{\frac{t-2t_2}{m}} \frac{a}{m^2} = \frac{a}{2m\gamma} e^{-\frac{\gamma t}{m}}, \end{aligned}$$

where we used Eq. (3.14) and the fact that the integration commutes with the average (we are allowed to flip the order). By comparing this with the equipartition theorem we get

$$\begin{aligned} \frac{1}{2}m\langle v^2 \rangle &= \frac{k_B T}{2} \\ \frac{1}{2}m\langle v(0)v(0) \rangle &= \frac{a}{4\gamma} = \frac{k_B T}{2} \\ a &= 2\gamma k_B T \end{aligned}$$

We notice the appereance of γ meaning that the magnitude of the fluctuations increase both with friction and temperature. Further we can integrate the velocity over time to get displacement $x(t)$ and show that the variance (show this? In appendix maybe?) is

$$\langle x^2(t) \rangle = \frac{2k_B T}{\gamma} \left(t - \frac{m}{\gamma} \left(1 - e^{-\gamma t/m} \right) \right),$$

where for $t \gg m/\gamma$ only the t -term survies yielding

$$\langle x^2(t) \rangle = 2k_B T t / \gamma.$$

In 1D, the diffusion constant D is related to the variance as $\langle x^2 \rangle = 2Dt$, meaning that this represents the einstein relation $D = \mu k_B T$ with the mobility $\mu = 1/\gamma$.

when $t \ll m/\gamma$ we use the Taylor expansion $1 - e^{-x} \approx x - x^2/2$ for $x \ll 1$ to get

$$\langle x^2(t) \rangle = \frac{k_B T}{m} t^2$$

which exactly matches the thermal velocity

$$v_{\text{th}} \frac{\langle x^2(t) \rangle}{t^2} = \frac{k_B T}{m}$$

which follows from the equipartition theorem. The finite correlation time γ/m hence describe the crossover from the ballistic regime $\sqrt{\langle x^2(t) \rangle} \propto t$ to the diffusive regime $\sqrt{\langle x^2(t) \rangle} \propto \sqrt{t}$.

Introduce the fluctuation-dissipation theorem concept earlier since this is a motivaiton for the Langeivn equation.

3.3.2 Implementing Langevin

The implementation of the Langevin equation into LAMMPS follows [74] and updates the force vector for each particle as

$$\begin{aligned} \mathbf{F} &= \mathbf{F}_c + \mathbf{F}_f + \mathbf{F}_r \\ &= -\nabla U - \gamma m \mathbf{v} + \sqrt{\frac{2k_B T m \gamma}{\Delta t}} \mathbf{h}(t) \end{aligned} \quad (3.15)$$

where \mathbf{F}_c is the conservative force computed via the usual inter-particle interactions described by the potential U , \mathbf{F}_f is the drag force and \mathbf{F}_r is the random fluctuation force where \mathbf{h} is a random vector drawn from a normal distribution with zero mean and unit variance. Notice that this generalized description of the Langevin equation deviates from the presentation in Eq. (3.12) since we have added the conservative force \mathbf{F}_c , but also by the appearance of the mass in both the drag force and the fluctuation force due to the introduction of damping. It is beyond out scope to comprehend this. However, the fact that Δt now appears in the denominator for the random force variance $2k_B T m \gamma / \Delta t$ is due to the fact that we have discretized time. This in agreement with the formulation in Eq. (3.13). By applying Eq. (3.15) we get the refined velocity verlet scheme

$$\begin{aligned} \mathbf{v}_i(t + \Delta t/2) &= \mathbf{v}_i(t) - \frac{\Delta t}{2} \left(\frac{\nabla_i U(t)}{m_i} + \gamma \mathbf{v}_i \right) + \sqrt{\frac{k_B T \gamma \Delta t}{2m_i}} \mathbf{h}_i \\ \mathbf{r}_i(t + \Delta t) &= \mathbf{r}_i(t) + \mathbf{v}_i(t + \Delta t/2) \Delta t \\ \mathbf{v}_i(t + \Delta t) &= \mathbf{v}_i(t + \Delta t/2) - \frac{\Delta t}{2} \left(\frac{\nabla_i U(t + \Delta t)}{m_i} + \gamma \mathbf{v}_i(t + \Delta t/2) \right) + \sqrt{\frac{k_B T \gamma \Delta t}{2m_i}} \mathbf{h}_i \end{aligned}$$

with new random vector \mathbf{h}_i for each particle and each update. Notice however, that LAMMPS only apply this scheme to the particle groups with the thermostat on.

3.4 MD limitations (?)

3.5 LAMMPS

Part II

Simulations

Chapter 4

Pilot study

4.1 Friction simulation parameters

The friction simulation is governed by a set of parameters where some is kept constant while other is varied to gain insight in the frictional properties. These parameters can be categorised into three main categories of different purpose as described in Table 4.1.

Table 4.1: Parameters of the numerical procedure for measuring friction.

Category	Parameter name: description	Category purpose
Physical	<ul style="list-style-type: none"> - T: Temperature for the Langevin thermostat. - v_{slide} : Sliding speed for the sheet translation. - K: Spring constant for the spring force between the virtual atom and the pull blocks responsible for translating the sheet along the substrate. An infinite spring constant is achieved by moving the pull blocks as a rigid body (Lammps: fix move). - Scan angle: The direction for which we translate the sheet. 	Parameters expected to have a physical effect on the friction properties, which is kept fixed and thus not included in the machine learning input set.
Measurement	<ul style="list-style-type: none"> - dt: Integration timestep. - t_R: Relaxation time before stretching. - Pauses between stretch and adding normal force and between dragging the sheet. - Stretch Speed: How fast to stretch the sheet. - Slide distance: How far to translate the sheet. - Sheet size: Spatial size of the 2D sheet. - Pull block size: spatial size of the pull blocks. 	Parameters influencing the simulation dynamics and being representative of the experimental procedure that we are mimicking. These parameters are chosen with the aim of getting stable parameters under small perturbations of the given parameter.
ML input	<ul style="list-style-type: none"> - Sheet configuration: A binary matrix containing information of which atoms are removed (0) and which are still present (1) in the graphene sheet. - Stretch amount: The relative sheet stretch in percentage. - F_N: Applied normal force to the pull blocks. 	The remaining parameters serve as input variables for optimization process and is thus given as input variables for the machine learning (ML).

Due to the great number of parameters, and corresponding range of reasonable numerical values they can take, it is ... to parameter search including all of these. Thus, we will to a great extent rely on a reverse engineering in order to establish a set of parameters for the *physical* and *measurement* categories along with numerical ranges for the *ML input* category which gives stable and promising results. By doing so we effectively narrow down the parameter regime for which the investigated frictional properties belong. We aim to choose the parameters in order to accommodate a balance between generalizable and stable result which is simultaneously a suitable candidate as a proof of concept for the control of friction properties using kirigami inspired cuts.

In the following we present the results of the friction simulations in parallel to the procedure of investigating the choice of different parameters.

In the following subsections (X to Y) we are going to present the friction simulation results in parallel to the presentation of the reasoning behind the parameter choices. For this we will refer to the default parameter choice showcased in Table 4.2 which is representative of the final parameter choices.

Table 4.2: Final parameters for the friction simulations Probably not the neatest format for this...

Physical	Measurements	ML input
$T = 300 \text{ K}$ $v_{\text{slide}} = 20 \text{ m/s}$ $K = \text{inf}$ (LAMMPS: <i>fix move</i>) Scan angle : $(x, y) = (0, 1)$	$dt = 1 \text{ fs}$ $t_R = 15 \text{ ps}$ Pauses = 5 ps Stretch speed = 0.01 ps^{-1} Slide distance = 400 \AA Sheet size = $130.029 \times 163.219 \text{ \AA}$ Pull block size = $2 \times 130.029 \times 15.183 \text{ \AA}$	Sheet configuration = Contiguous Stretch amount = Below rupture $F_N = [0.1, 10] \text{ nN}$

Say something about how these parameters are chosen. Reference to articles for which these were mirrored from.

4.1.1 Pressure reference for normal load domain

Find place to put this.

In order to relate the magnitude of the normal force in our friction measurement we will use the pressure as a reference. We will use the pressure underneath a stiletto shoe as a worst case for human pressure execution underneath the shoe. From (source 1) it is reported that the diameter of a stiletto heeled shoe can be less than 1 cm. Hence a 80 kg man³ standing on one stiletto heel (with all the weight on the heel) will result in a pressure

$$P = \frac{F}{A} = \frac{mg}{r^2\pi} = \frac{80 \text{ kg} \cdot 9.8 \frac{\text{m}}{\text{s}^2}}{(\frac{1 \times 10^{-2} \text{ m}}{2})^2\pi} = 9.98 \text{ MPa}$$

While this is in itself a spectacular realization that is often used in introductory physics courses (source 2) to demonstrate the rather extreme pressure under a stiletto heel (greater than the foot of an elephant) (how many Atmos?) this serves as a reasonable upperbound for human executed pressure. With a full sheet area of $\sim 21 \times 10^3 \text{ \AA}^2$ we can achieve a similar pressure of $\sim 10 \text{ MPa}$ with a normal force of

$$F_N = 10 \text{ MPa} \cdot 21 \times 10^{-17} \text{ m}^2 = 2.10 \text{ nN}$$

Of course this pressure might be insufficient for various industrial purposes, but with no specific procedure in mind this serves as a decent reference point. Notice that if we consider a human foot with area 113 cm^2 the pressure drops to a mere 70 kPa corresponding to $\sim 0.01 \text{ nN}$.

³Yes, a man can certainly wear stiletto heels.

4.2 Single friction simulation analysis

We begin by assessing the raw data for a single friction simulation run with the default parameters shown in Table 4.2 for a non-cut sheet, no stretch and an applied normal force of 1 nN.

4.2.1 Force oscillations

We first assess the raw data for the friction force F_{\parallel} parallel to the drag direction as seen in Fig. 4.1. The sample rate is $10 \text{ ps}^{-1} = 100 \text{ timesteps}^{-1}$ for which each sample is the mean value of the 100 timesteps preceding the given sample interval. We observe immediately that the data carries oscillations on different time scales. By applying a savgol filter to the data with a polyorder of 5 and window length of 150 timesteps, corresponding to a sliding distance of 3 Å or a time window of 15 ps, we can qualitatively point out at least two different frequencies of oscillation. On Fig. 4.1a we see roughly three waves on the savgol filter corresponding to a relative high frequency, while on Fig. 4.1b the same savgol filter reveals a lower frequency on top of the first, creating the visual pattern of a wavepacket.

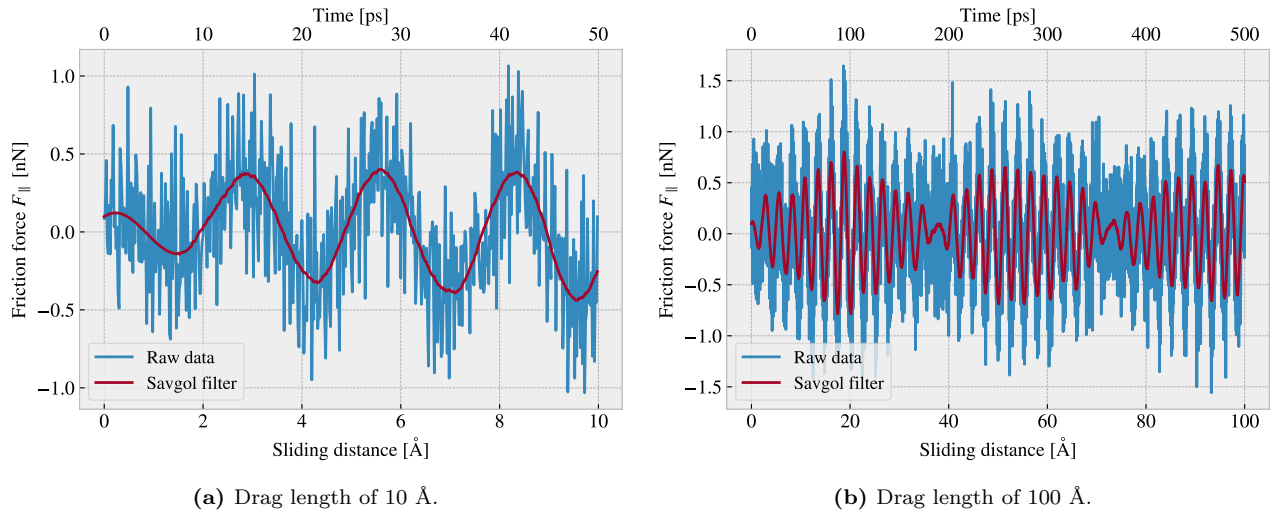


Figure 4.1: Friction force F_{\parallel} with respect to the drag direction between (full) sheet and substrate versus sliding distance. The sliding distance is measured by the constant movement of the virtual atom and not the COM of the sheet. However, we expect these measures to be fairly identical due to the fact that the pull blocks are rigidly coupled to the virtual atom. The red line represents a savgol filter with window polyorder 5 and window length of 150 timesteps (corresponding to a sliding distance of 3 Å or a time window of 15 ps).

By performing a Fourier Transform (FT) on the data we can quantify the leading frequencies as seen in Fig. 4.2a. By plotting the two most dominant frequencies $f_1 = 0.0074 \text{ ps}^{-1}$ and $f_2 = 0.0079 \text{ ps}^{-1}$ as $\sin(2\pi f_1) + \sin(2\pi f_2)$ we find a qualitatively convincing fit to the observed wavepacket shape as seen in Fig. 4.2b. By using the trigonometric identity

$$\begin{aligned}\sin(\alpha + \beta) &= \sin(\alpha)\cos(\beta) + \cos(\alpha)\sin(\beta), \\ \sin(\alpha - \beta) &= \sin(\alpha)\cos(\beta) - \cos(\alpha)\sin(\beta),\end{aligned}$$

and decomposing $f_1 = a - b$, $f_2 = a + b$ we can rewrite the sine sum as the sinusoidal product

$$\begin{aligned}\sin(2\pi f_1)\sin(2\pi f_2) &= \sin(2\pi(a - b))\sin(2\pi(a + b)) \\ &= \sin(a)\cos(b) + \cancel{\cos(2\pi a)\sin(2\pi b)} + \sin(2\pi a)\cos(2\pi b) - \cancel{\cos(2\pi a)\sin(2\pi b)} \\ &= 2\sin(2\pi a)\cos(2\pi b),\end{aligned}$$

with

$$\begin{aligned}a &= \frac{f_1 + f_2}{2} = 0.0763 \pm 0.0005 \text{ ps}^{-1}, & b &= \frac{f_2 - f_1}{2} = 0.0028 \pm 0.0005 \text{ ps}^{-1}, \\ &= 0.381 \pm 0.003 \text{ Å}^{-1}, & &= 0.014 \pm 0.003 \text{ Å}^{-1},\end{aligned}$$

where the latter frequency is denoted with respect to the sliding distance. This makes us recognize the high oscillation frequency as a and the low frequency as b . The faster one has a period of $T_a = 2.62 \pm 0.02 \text{ \AA}^4$. This corresponds well with the magnitude of the lattice spacing and especially that of graphene at 2.46 \AA as expected theoretically (make reference to theory section?). We also take note of the longest period $T_b = 71 \pm 15 \text{ \AA}^{-1}$ which will be relevant for the evaluation of measurement uncertainty in section Sec. 4.3.

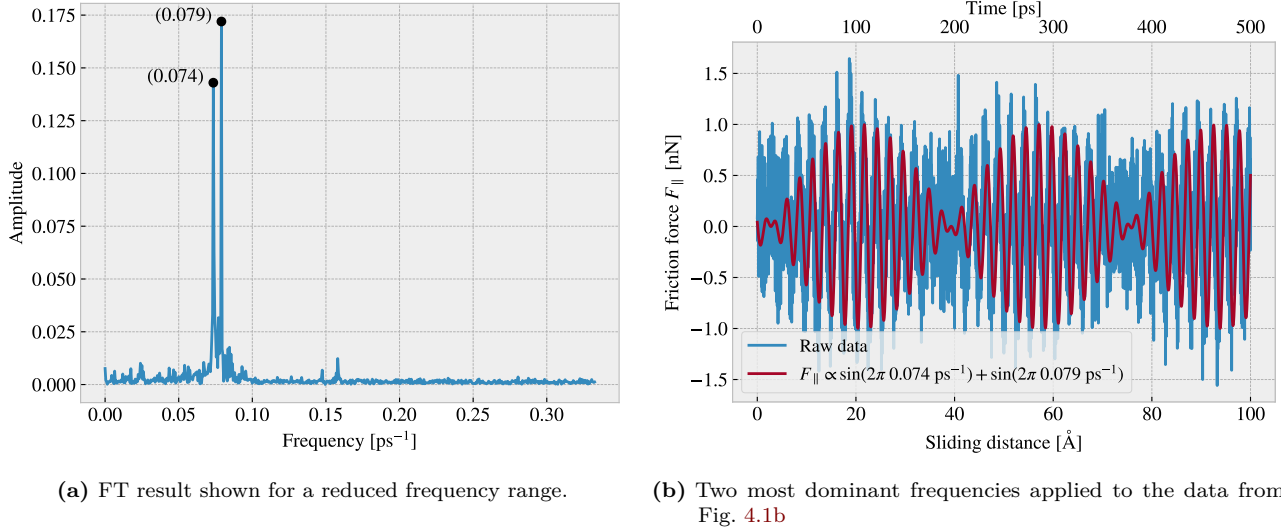


Figure 4.2: Fourier transform (FT) analysis of the full friction force data (all 400 \AA sliding distance) shown in Fig. 4.1. (a) shows the two most dominant frequency peaks. Note that no significant peaks were found in a higher frequency than included here. (b) shows a comparison between the raw data and the wavefunction corresponding to the two peaks in figure (a).

4.2.2 Decompositions

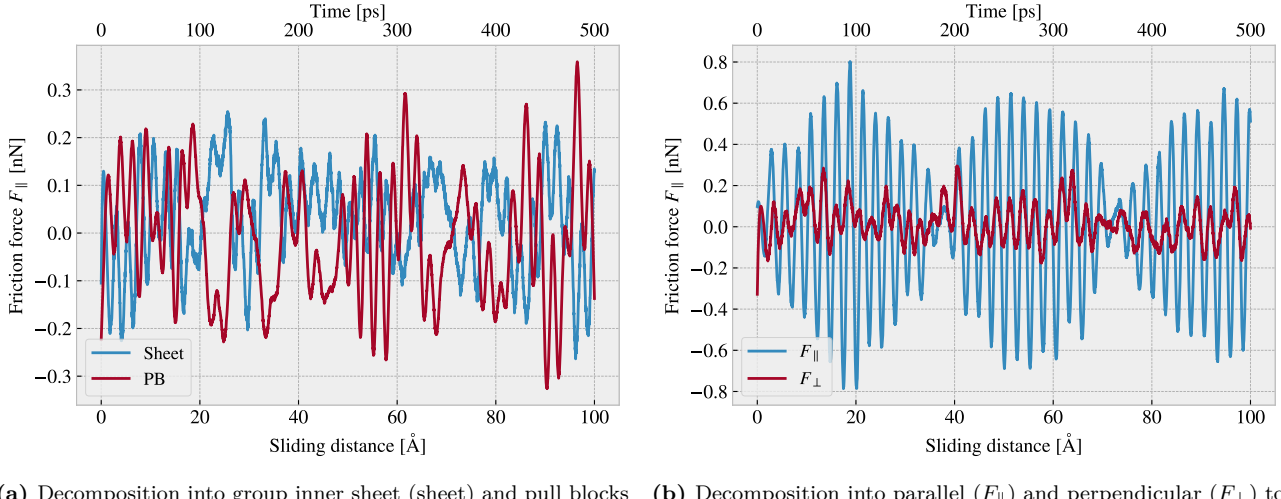
In the previous analysis we have looked only at the friction force for the full sheet, including the pull blocks which is locked off during sliding, and with respect to the drag direction. This represents our choice measurement which we will address in the following.

Due to the fact that we are only applying cuts to the inner sheet (excluding the pull blocks), it might seem more natural to only consider the friction on that part. If the desired frictional properties can be achieved by altering the inner sheet one can argue that any opposing effects from the pull blocks can be mitigated by scaling the relative size between the inner sheet and the pull blocks. However, when looking at the time series of the friction force decomposed with respect to the inner sheet and pull block region (see figure Fig. 4.3a), we observe the friction force arising from those parts are seemingly antisymmetric. That is, the distribution of the frictional pull from the substrate on the sheet is oscillating between the inner sheet and the pull block. Keeping in mind that normal force is only applied to the pull blocks we might take this as an integrated feature of the system which does not necessarily disappear when changing the spatial ratio between inner sheet and pull block. Any interesting friction properties might depend on this internal distribution of forces. Hence, we hedge our bets and use the full sheet friction force as a holistic approach to this measurement problem.

Similar we might question the decision of only considering the frictional force projected onto the sliding direction as we are neglecting the “side shift” induced during the slide phase. In Fig. 4.3b we see the decomposition into force components parallel F_{\parallel} and perpendicular F_{\perp} to the slide direction respectively. We see that the most dominant trend is projected into the parallel component. If we want to include the perpendicular component as well we would have to evaluate the friction as the length of the force vector for which we would lose the sign of the force direction. Hence, we would only get a positive contribution which would not be able to capture the change between resisting and assisting the sliding during stick-slip motion. One option to accommodate this is by using the vector length but keeping the sign from the projection parallel to the sliding direction. However, we

⁴The uncertainty Δy is calculated as $\Delta y = \left| \frac{\partial y}{\partial x} \Delta x \right|$ for uncertainty Δx and $y(x)$

omit such compromises as this might make analysis interpretation more difficult, and we use only the parallel component going forward.



(a) Decomposition into group inner sheet (sheet) and pull blocks (PB). (b) Decomposition into parallel (F_{\parallel}) and perpendicular (F_{\perp}) to drag sliding direction.

Figure 4.3: Friction force decomposition on the data shown in Fig. 4.1 with applied savgol filters similar to that of Fig. 4.1b with window polyorder 5 and window length of 150 timesteps (corresponding to a sliding distance of 3 Å or a time window of 15 ps).

4.2.3 Center of mass path

From the previous observations of the friction force time series we see evidence of a stick-slip behaviour. Specially, we see in Fig. 4.3b that this might be the case both parallel and perpendicular to the sliding direction. By looking at the x, y -position for the sheet center of mass (COM) we observe the stick-slip motion manifested as a variation in COM speed combined with a side to side motion as shown in figure Fig. 4.4a. In an attempt to increase the magnitude of the slips we evaluate a similar simulation with spring constant $K = 30 \text{ N/m}$ (see figure Fig. 4.4b) in contrast to that of an infinite spring constant. While the maximum slip speed stays within a similar order of magnitude the slip length in the sliding direction is increased along with the side to side motion. Note that the axis scale is different between Fig. 4.4a and Fig. 4.4a. However, in both cases we observe that the side to side motion is associated with a low speed, meaning that is more reminiscent of a “slow” creep alignment with the substrate than a slip.

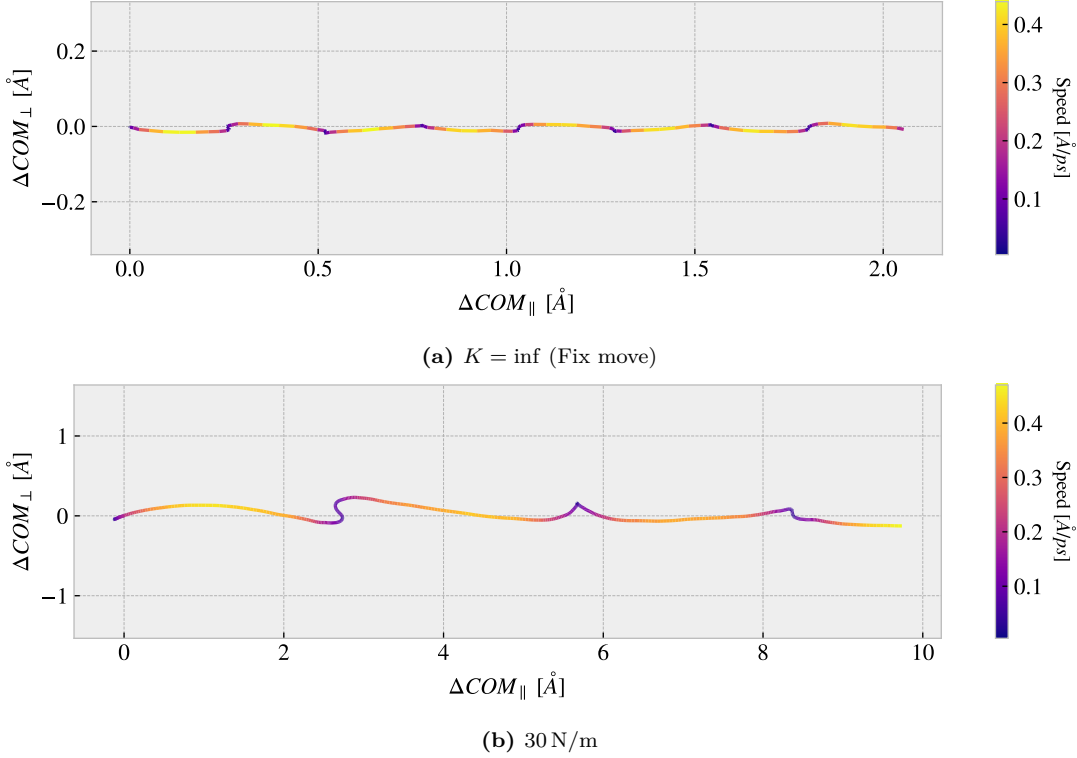


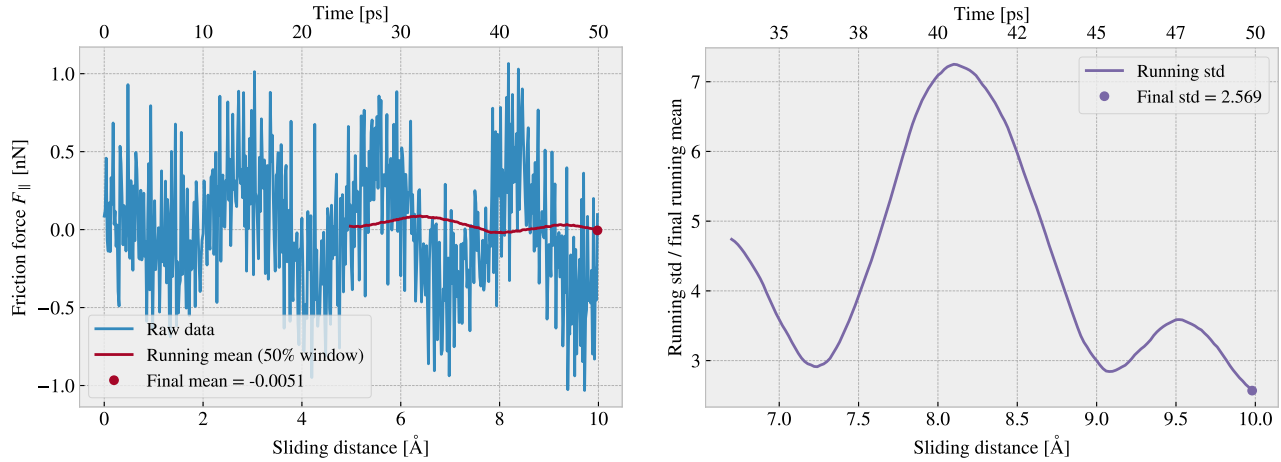
Figure 4.4: Center of mass position relative to the start of the sliding phase in terms of the direction parallel to the sliding direction ΔCOM_{\parallel} and the axis perpendicular to the sliding direction ΔCOM_{\perp} . The colorbar denotes the absolute speed of the COM.

4.3 Defining metrics for dynamic and static friction

In order to evaluate the frictional properties of the sheet we reduce the comprehensive friction force time series addressed in section Sec. 4.2 into single metrics describing the dynamic and static friction. The natural choice is to use the mean and max values of the time series.

4.3.1 Dynamic friction

For the dynamic friction measurement we take the mean value of the latter half of the dataset to ensure that we are sample from a stable system. For a full sliding simulation of 400 Å we thus base our mean value on the latter 200 Å of sliding. In Fig. 4.5a we have shown the friction force of the first 10 Å of sliding together with a running mean with window length of 5 Å corresponding to 50% the data length. This is merely done to illustrate the sampling procedure and by only using a 10 Å sliding distance the final mean estimate (indicated with a dot) takes a negative value due to the specific cut-off of the few oscillations captured here. Nonetheless, one approach to quantify the uncertainty of the final mean estimate is to consider the variation of the running mean preceding the final mean value. The more the running mean fluctuates the more uncertainty associated with the final estimate. However, only the running mean “close” to the ending should be considered, since the first part will rely on data from the beginning of the simulation. From the Fourier analyse in section Sec. 4.2.1 we found the longest significant oscillation period to be $\sim 71 \text{ \AA}^{-1}$ corresponding to $\sim 35\%$ of the running mean window consisting of 200 Å of slifing when including all the data. Hence, we use the standard deviation of the final 35% of the running mean to approximate the uncertainty of the final mean value, and we estimate the relative error by dividing the standard deviation by the final mean value. In Fig. 4.5b we showcase a running standard deviation of a window length 35% the running mean window in Fig. 4.5a for the illustrative case of a total 10 Å slide. The final uncertainty value is marked by a dot, and we see as expected that we get a high relative error of $\sim 257\%$ which corresponds well with the short sampling period and the mean value taking an unphysical negative value.



(a) Running mean with window length 5 Å (50% the data length). (b) Running std with window length 1.75 Å (35% the mean window length.)

Figure 4.5: Running mean and running standard deviation (std) on the friction force data from a 10 Å of sliding simulation. The running mean window is 50% the data length while the running std window is 35% the running mean window length.

When including the full dataset of 400 Å of sliding, such that std window actually matches with the longest period of oscillations expected from the data, we get a final relative error of $\sim 12\%$ as shown in Fig. 4.6. This is arguable just at the limit for an acceptable error, but as we shall see later (Make a reference to fig or sec) this high relative error is mainly connected to the cases of low friction. When changing the simulation parameters, such that the mean friction evaluates to considerable higher values, the relative error drops to the order (put in numbers). One interpretation of this finding is simply that the oscillations in the running mean is somewhat independent of the magnitude of the friction. In that case, the relative error will spike for the low friction cases.

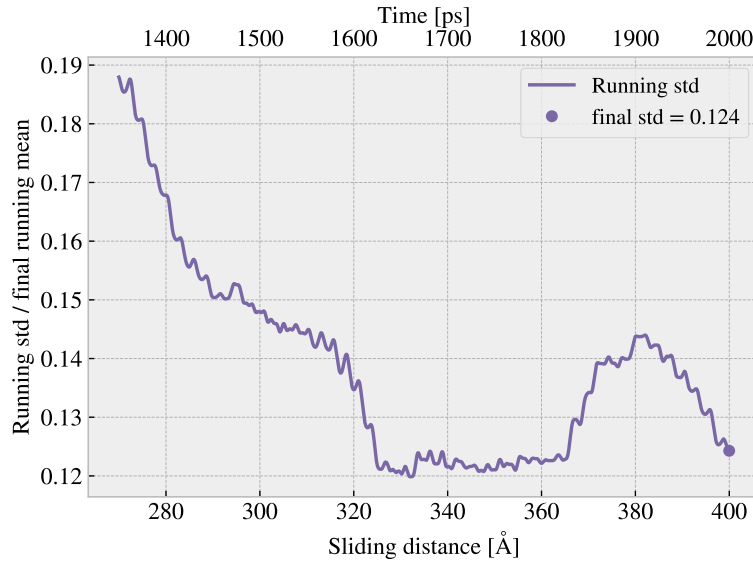


Figure 4.6: Running standard deviation (std) for a full 400 Å sliding simulation. The running std window is 70 Å (35% the running mean window of 50% the data length).

4.3.2 Static friction

The max value is the most obvious choice for addressing the static friction, even though that the definition of the static friction is a bit vague. When considering the friction force time series in Fig. 4.1 we observe that the

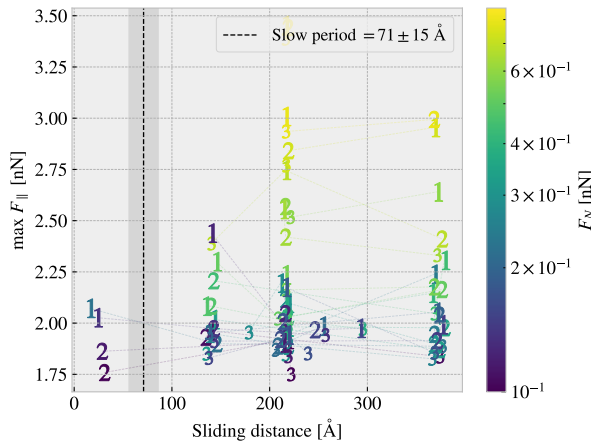


Figure 4.7: Distribution of top three max friction force peaks for 30 uniformly sampled normal forces $F_N \in [0.1, 10]$ nN. The dotted line and the grey area marks the slowest significant oscillation period found in the data and thus marking a dividing line for whether a peak falls within the “beginning” of the sliding simulation.

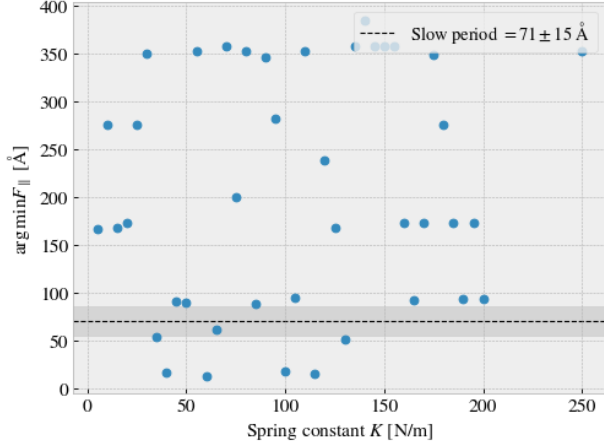


Figure 4.8: Sliding displacement for the max friction peak to appear as a function of spring constant. Fixmove is tmp mapped to $K = 200$ here without any discontinuous lines.

stick-slip oscillations increase in magnitude toward a global peak at ~ 20 Å. Thus, we could identify this peak as the static friction force, but the global max does in fact rarely fall within the first part of the sliding. In Fig. 4.7 we investigate the top three max value, at which sliding distance they occur and at what magnitude, for 30 uniformly sampled normal forces in the interval [0.1, 10] nN. It is immediately clear that only few of the peaks falls within the “beginning” of the simulation defined by the slowest significant oscillation period of 71 ± 15 Å. In fact only 2/30 global values and 4/90 top three values can be associated to the start of the sliding by this definition. Thus, this result suggests that the max value cannot be used as a reliable measure for the static friction either due to its lack of presence or due to the simulation setup procedure. For a more typical evaluation of the static friction force one would increase force slowly until the first slip significant slip is recorded (a series of precursors is expected to precede this). In our simulations we drag the sheet relatively fast in a rigid manner which might be the reason for the lacking the static friction. Bonelli et al. [56] reported that the stick-slip behaviour was only presented when using a relatively soft spring. Thus, by changing the spring constant we investigate possibility to observe a static friction (**I kind of interchanged stick-slip and static friction int his argument, but I still think it can be used to argue for doing the test...**) response within the framework of our simulation procedure as shown in Fig. 4.8. However, the results do not indicate any implications that a recognizable domain exist for which the static friction response would be reliable. Hence, we will base the final assessment on frictional properties purely on the dynamic friction force.

4.4 Out of plane buckling

The out of plane buckling is the main motivation for applying the kirigami inspired cuts to the sheet. Thus, we perform a stretch simulation in a low temperature $T = 5$ K vacuum in order to verify that the chosen cut configurations do in fact contribute to a significant out of plane buckling when stretched. For the non-cut, popup and honeycomb configuration we assess the movement in the z-direction (perpendicular to the plane) during the stretch, which we visualize by the min and max z-value along with the atom count quartiles 1%, 10%, 25%, 50% (median), 75%, 90% and 99% as shown in figure Fig. 4.9. We observe that the popup and honeycomb pattern buckles considerable out of plane during the stretch in comparison to the non-cut sheet which only exhibit minor buckling of ~ 2 Å which is on the same order as the atomic spacing in the sheet. We also notice that the popup pattern buckles more in consideration to the min and max peaks while the 1%, 99% quartiles is on the same

magnitude as the honeycomb. By looking at the simulation visualization ([include OVITO figures for vacuum stretch as well?](#)) we can conclude that this is mainly due to the fringes of the sheet “flapping” around.

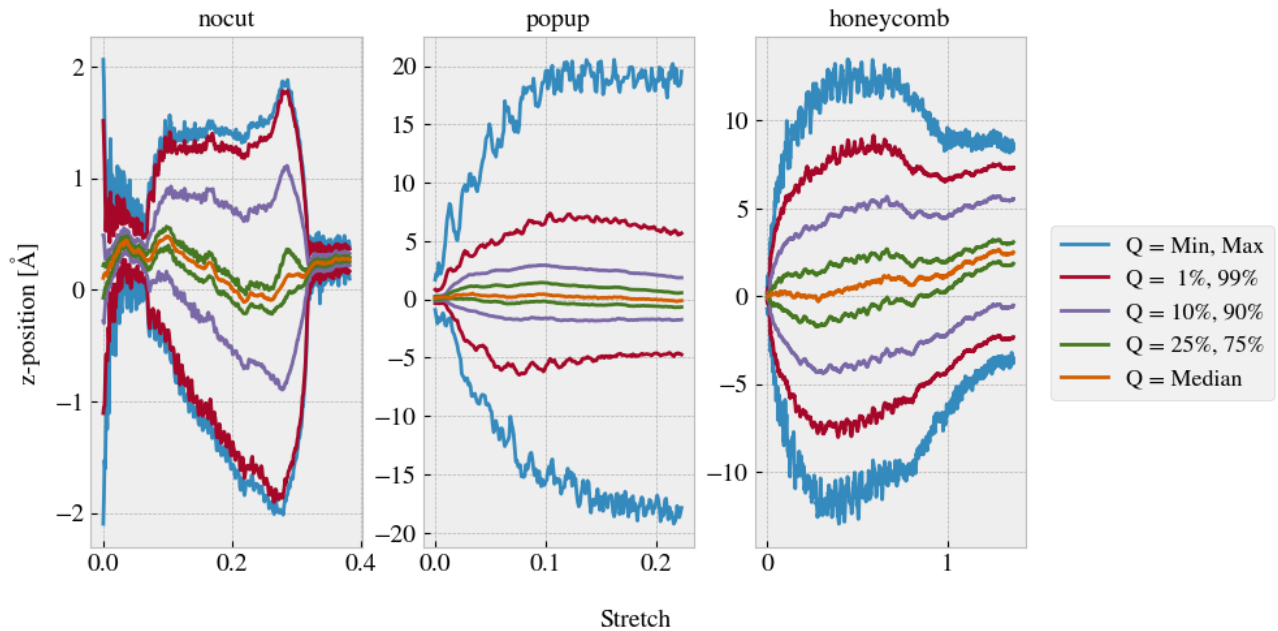


Figure 4.9: Out of plane buckling during stretch of sheets in vacuum at $T = 5$ K. Reading from left to right the vacuum rupture stretch are 0.38, 0.22 and 1.37. [perhaps use a color scale instead of the standard color cycles here.](#)

The next step is to verify that the buckling will lead to a significant altering of the contact area when the sheet is in put in contact with the substrate. We investigate this by simulating the stretch at the default temperature $T = 300$ K with the presence of contact forces between the sheet and substrate. Note that no normal load is applied as the sheet and substrate is sufficiently attracted by the LJ potential. Selected frames from the simulation is shown in appendix [??](#). We assess the contact area by the relative amount of atoms in the sheet within chemical range of the substrate. The cut-off for this interaction is 4 \AA corresponding to $\sim 120\%$ the LJ equilibrium distance. Since the contact area is usually calculated as the amount of atoms in contact multiplied with an associated area for each contact this feature is taken to be proportional to the contact area. The relative amount of bonds as a function of stretch for the various configurations is shown in figure Fig. 4.10 which clearly indicates a drop in contact area as the cutted sheets are stretched.

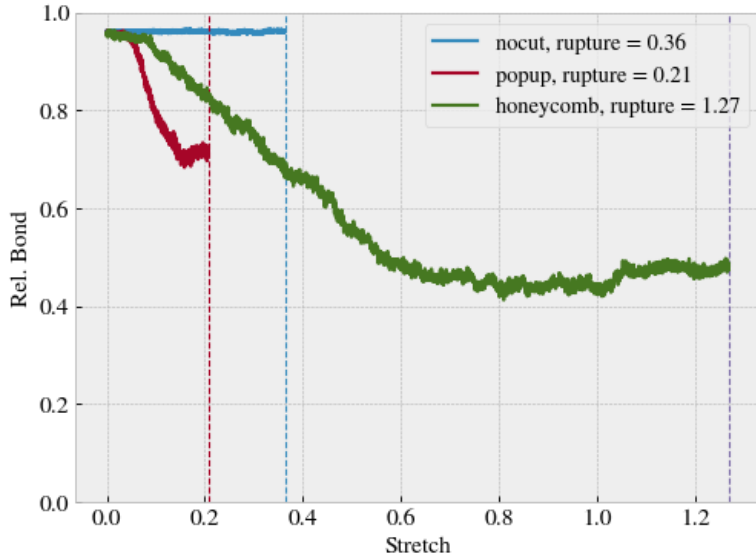


Figure 4.10: Contact vs. stretching of the sheet, where the contact is measured by the relative amount atoms in the sheet within chemical interaction range to the substrate. The cut-off for this interaction range is 4 Å corresponding to $\sim 120\%$ the LJ equilibrium distance. $T = 300$ K

Compare figure Fig. 4.10 to that of figure Fig. 4.15 where multiple simulations constitute the stretch-contact curve.

4.5 Investigating selected parameters

We investigate the importance of the physical variables T , v_{slide} and K (make plots for scan angle as well?) and the choice of timestep dt . This is done partly understand how the dependencies relate to theoretical, numerical and experimental results, and partly to understand how these parameter choices defines the regime for our multi configurational search. We use the default parameters in Table 4.2 with exception of the single parameter of interest which is varied in a reasonable range of the default choice. In Fig. 4.11-Fig. 4.14 the dynamic friction estimate and the max friction force is shown as a function of T , v_{slide} , K and dt respectively. For the dynamic friction estimate the absolute error is denoted by a shaded error which linearly connects the points.

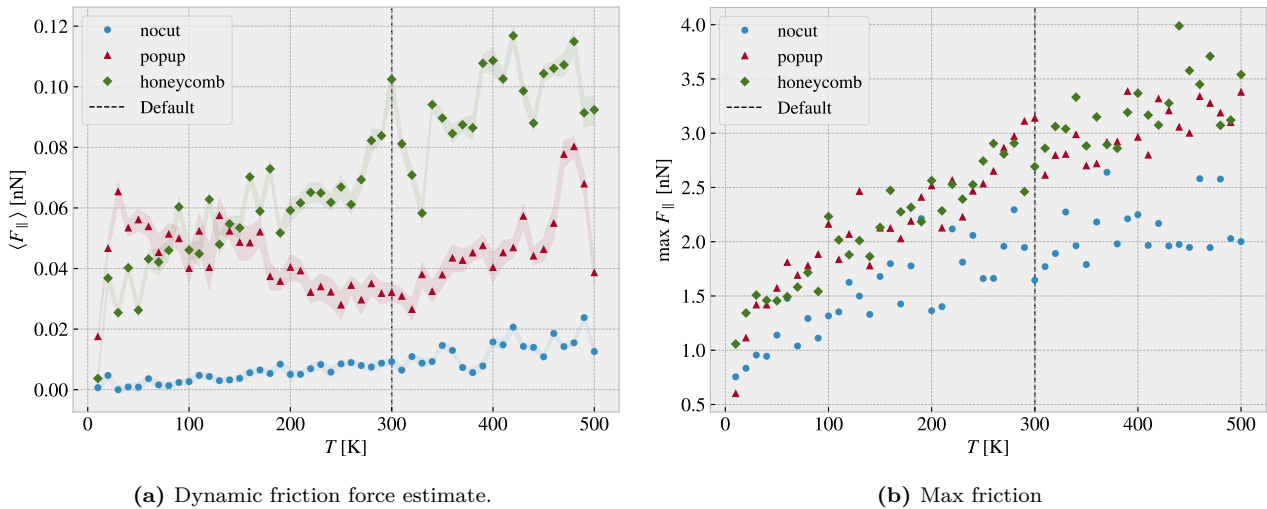


Figure 4.11: Temperature.

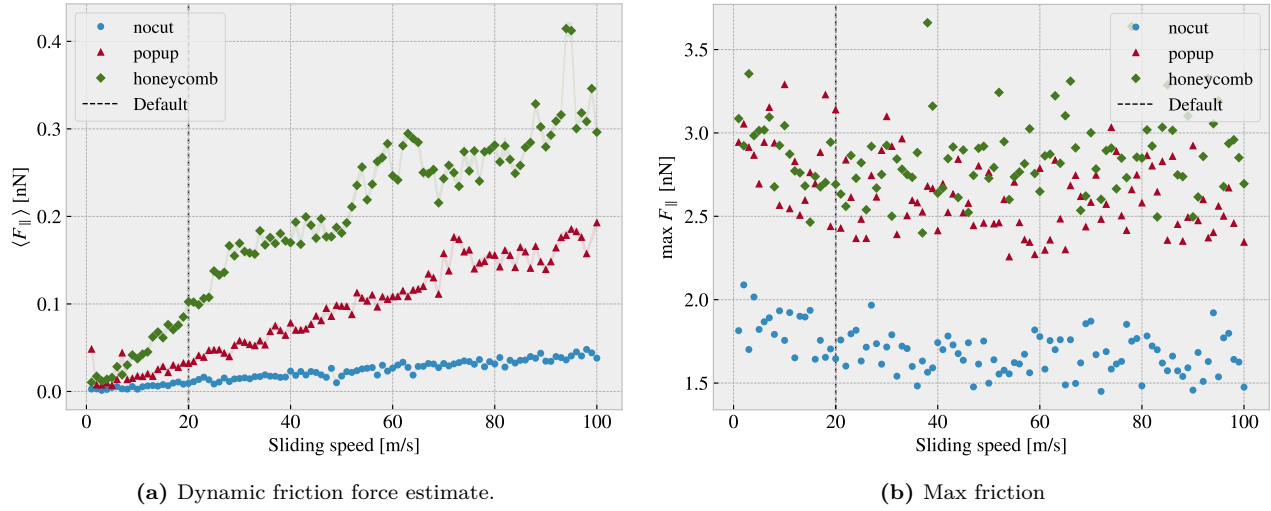


Figure 4.12: Sliding speed

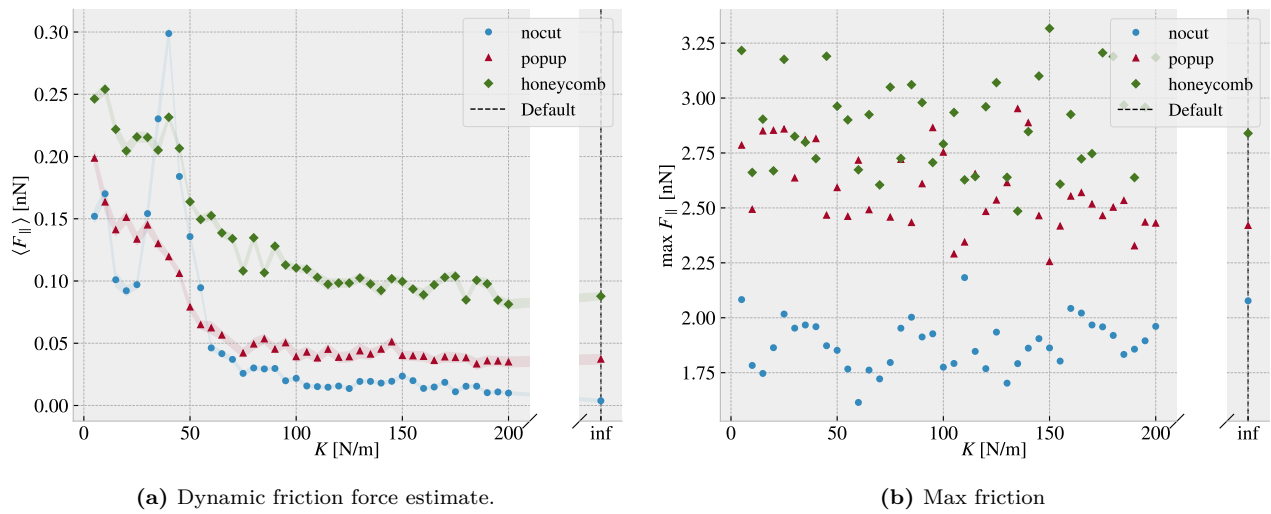


Figure 4.13: Spring constant

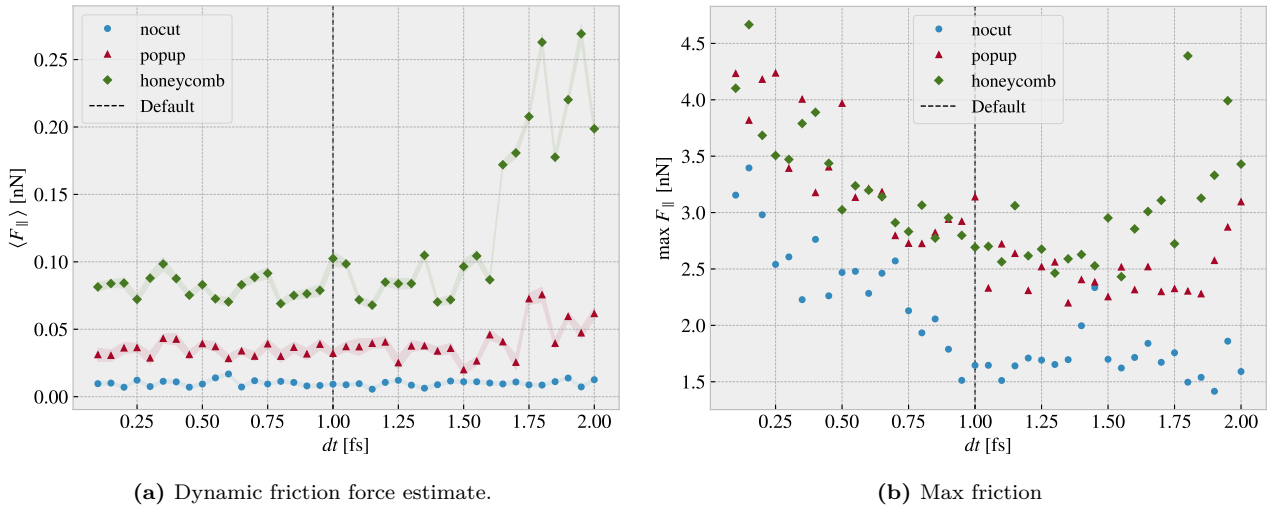


Figure 4.14: Timestep

Quick thoughts:

- Temperature: We do clearly not see the $1/T$ temperature decrease. The non-cut sheet seems to showcase a linear relationship which is also somewhat present for the honeycomb which matches some of the findings in other MD simulations. For the popup we do see a local decrease at low temperatures which flip at around the default $T = 300$ K temperature. The max friction peaks seem to increase with temperature as well indicating that the peaks might be associated with thermal fluctuations rather than actual stick-slip behaviour. This supports the finding that the static friction response is not significantly present in these simulations.
- Velocity: Considering the non-cut sheet first the velocity dependency is seemingly linear which deviates from the expected logarithmic trend. For the cutted configurations we find some peaks which might indicate the presence of resonance frequencies. The cutted sheet might be closer to a logarithmic trend, but this is not spot on either. The max friction seems to decrease slightly with small velocities and then stay rather constant. This can probably be explained by the reduced time to stick between stick slip.
- Spring constant: On all three configurations the dynamic friction decreases with an increasing spring constant. The best explanations might be due to the lack of freedom to “get stuck” in incommensurable configurations. We also notice that the friction varies a lot at lower spring constants supporting the choice of having a stiff spring for stability reasons. Especially the non-cut sheet peaks at $K = 40$ N/m. The max friction seem to be constant with K .
- dt : The dynamic friction is relatively stable around the default choice of $dt = 1$ fs. However, the fluctuations with respect to dt is more significant for popup pattern and even more for the honeycomb pattern. This indicates that the more complex dynamics of the simulation is more sensitive to the timestep. We might interpret this information as an additional measure of uncertainty. The maximum friction decreases with increasing timestep which can be asserted a statistical interpretation: Higher peaks will be captured by the high resolution of a low dt and vice versa. The high max values towards the point of $dt = 2$ fs is most likely due to the approach of instability in the simulation as seen more clearly for the dynamic friction evaluation.

4.6 Normal force and stretch dependencies

Till this point we have only changed variables one by one to investigate single dependencies. We now advance the study to a simultaneous variation of stretch and normal force.

Explain how the stretch is uniformly sampled within equally divided intervals and the normal force is actually uniformly sampled in a given range. Argue that the first might be approximately uniformly distributed for large numbers.

Talk about rupture test also. Maybe in the theory/method section under numerical procedure: Before simulating a rupture test is perform to determine under what stretch the sheet ruptures. This is a slightly higher threshold than when applied normal load and sliding along the substrate.

4.6.1 Contact area

??

We reproduce the contact area investigation of Fig. 4.10 with the modifcaiton that the contact count is measured as an average of the latter 50% of the sliding simulation at a non-zero applied normal load. The results are shown in Fig. 4.15 with 30 attempted (some rupture) stretch (pseudo) uniformly distributed stretch between 0 and the rupture point and 3 uniform distributed normal loads in the interval [0.1, 10] nN.

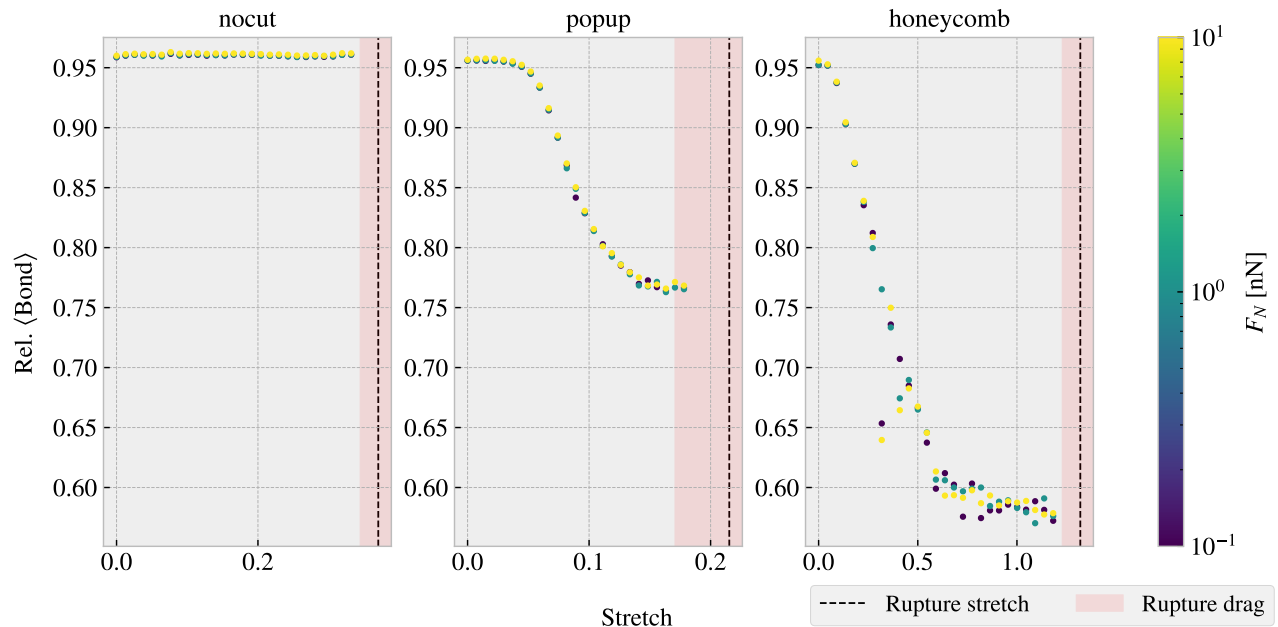


Figure 4.15: Average relative amount of bonds beetwen the sheet and the substrate defined by the cut-off distance of 4 Å. The average is taken over the latter half of the sliding phase. The red shade denotes the stretch range where ruptures accour at certain normal loads under sliding while the black-dotted line represent the rupture point due to stretching (rupture test)

From Fig. 4.10 we observe a significant decrease in the contact due to stretching of the cut configurations in contrast to the non-cut which stays roughly constant. This is reminiscent of the non-sliding stretch vs. contact curve shown in Fig. 4.10. Given these results, theoretically one would expect the dynamic friction to decrease with stretch for the cut configurations.

4.6.2 Stretch

We make a similar analysis as done in the previous section ?? with the substitution of friction force instead of contact (The data is taken from the same simulaitons runs). The dynamic friction force (put uncertainty here even though that it is quite low?) and the max friction is shown in Fig. 4.16a and Fig. 4.16 respectively.

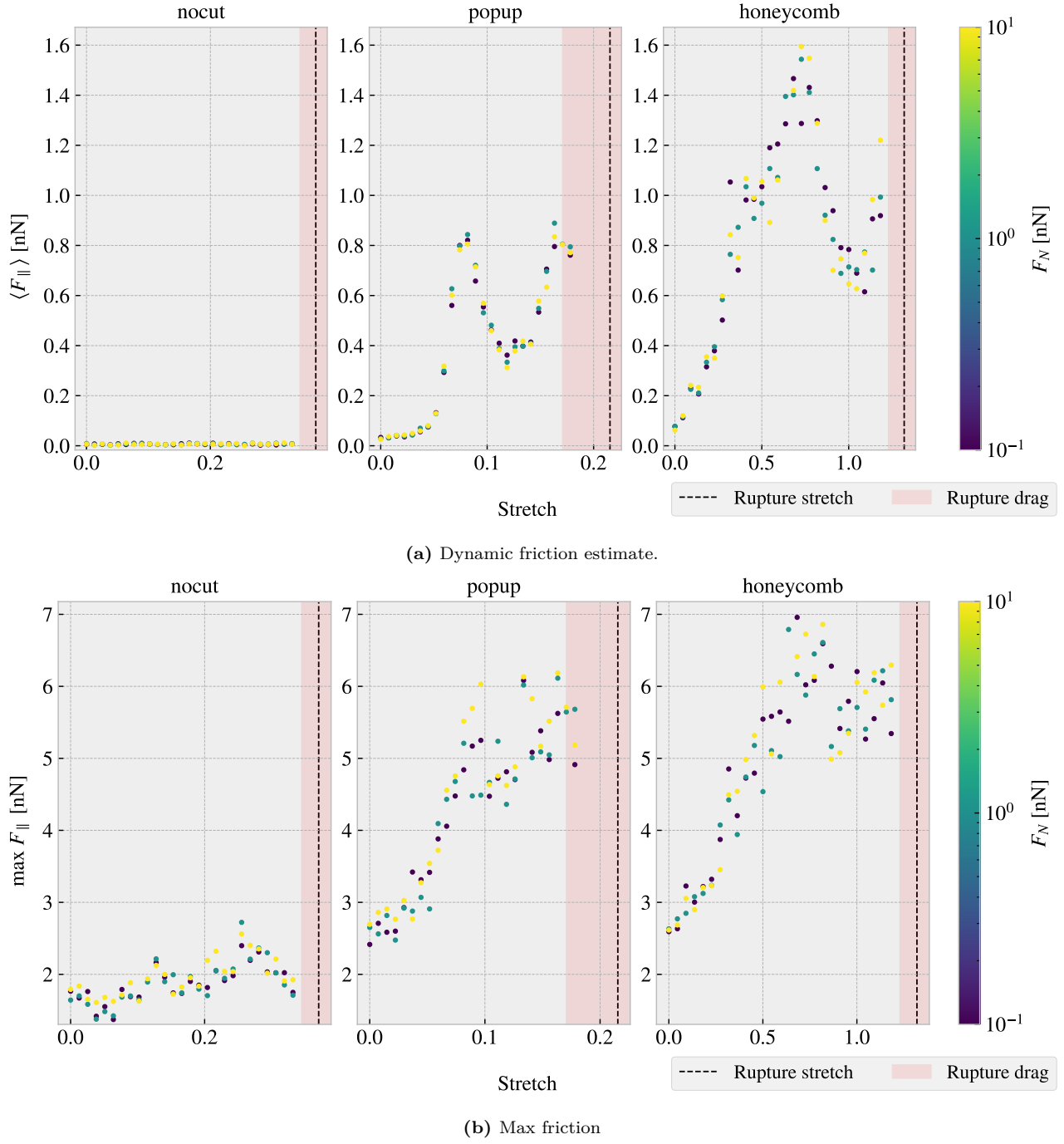


Figure 4.16: CAPTION

From Fig. 4.16a we find to our surprise that the dynamic friction increase with stretch for the cut configurations despite a simultaneous decrease in contact area as shown in figure Fig. 4.15. This suggests that the amount of chemical bonding atoms is not the dominant mechanism for the friction of this system. Instead, we might point to a mechanism more mechanical of nature associated to phonon excitations. When the cut sheet is stretched the stress (show stress maps somewhere or not necessary?) might induce a certain distribution and magnitude of point pressures to favor energy dissipation. Nonetheless, the results showcase a strong coupling between stretch and friction force, also for the max friction force, which is beyond the expectations at this stage of the study. The non-cut configuration does not show significant dependency on the stretch which reveal that this effect is only present when combining cut and stretch and not purely by stretching the sheet.

By considering the increase in dynamic friction towards the first peak we get a relative friction increase and increase vs. stretch ratios as described in Table 4.3. While the honeycomb force increase towards the first peak is approximately linear the popup exhibits seemingly exponential growth which yield a slope on the order ~ 30 nN.

Table 4.3: (stretch, dynamic friction) coordinates from Fig. 4.16a at start and the first peak respectively used to approximate the relative increase in friction force and the ratio for friction increase vs. stretch for sait range. In practice the latter ratio denotes the slope of a forced linear trend.

Configuration	Start	First peak	Relative increase	Friction force vs. stretch ratio [nN]
Popup	$\sim (0, 0.03)$	$\sim (0.082, 0.83)$	27.7	9.76
Honeycomb	$\sim (0, 0.07)$	$\sim (0.728, 1.57)$	22.4	2.06

Additionally, we notice that both the popup and honeycomb also exhibits stretch ranges where the dynamic friction force decrease with increasing stretch. Qualitatively we assign the slope to be on the same order of magnitude as those towards the first peak. This is useful for the prospect of taking advantage of this phenomena as we can essentially achieve both higher and lower friction for increasing stretch for different starting points.

4.6.3 Normal force

Main take away from this section should be that the normal force does not really change the friction much; The friction coefficient is extremely low, but I'm not sure how well the linear fits are (whether they are linear or sublinear). Not sure if I should do a linearly increasing normal force for better linear plots?

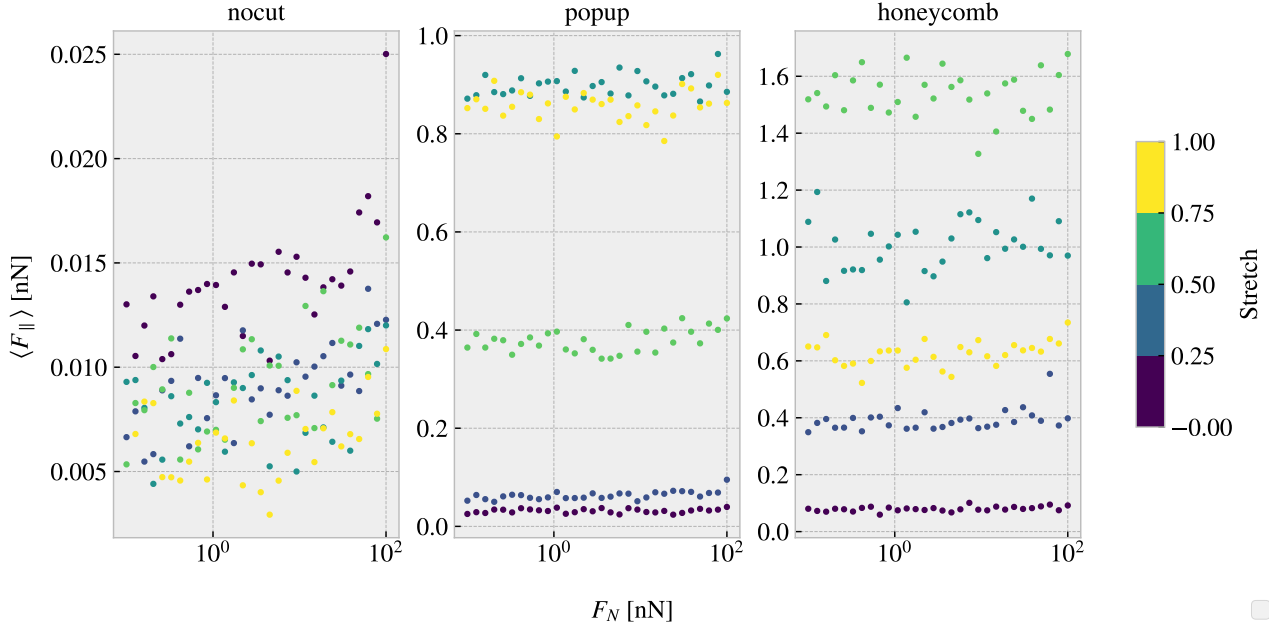


Figure 4.17: ...

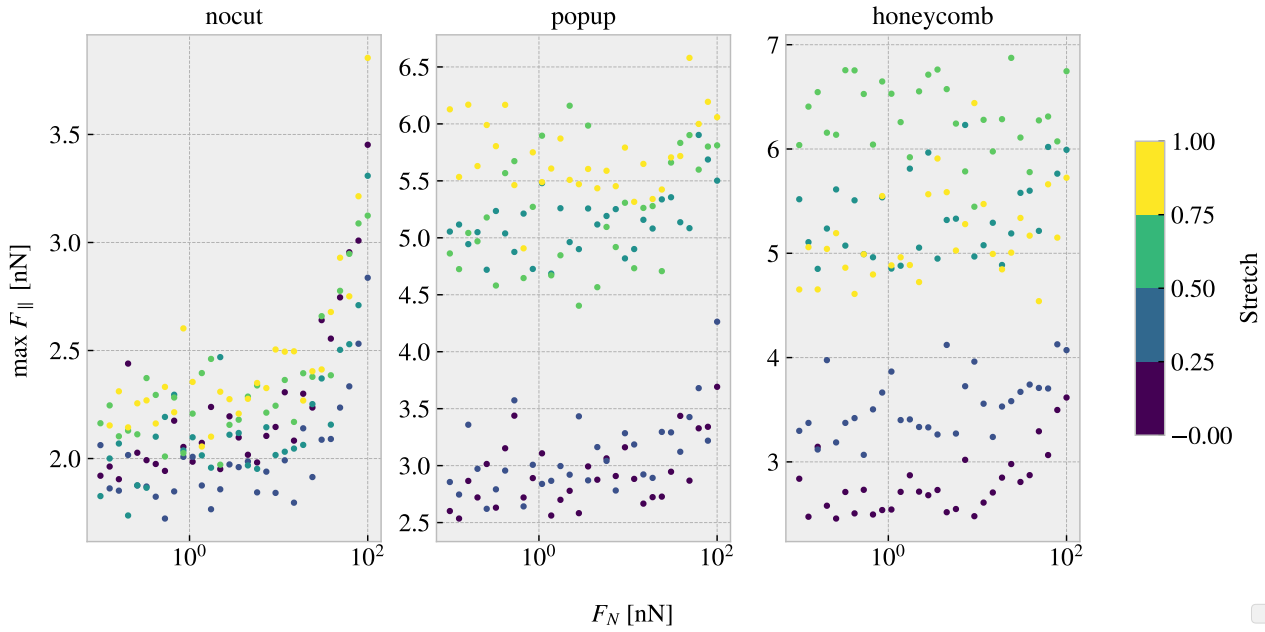


Figure 4.18: Colorbar is only fitted for the right plot (honeycomb)... this should be fixed. Should I have run a linear distribution of FN so I could plot it linear here also...?

Table 4.4: Mean friction coeff

nocut	$0.00009 \pm 1 \times 10^{-5}$	$0.00005 \pm 1 \times 10^{-5}$	$0.00004 \pm 1 \times 10^{-5}$	$0.00005 \pm 2 \times 10^{-5}$	
popup	$0.00005 \pm 3 \times 10^{-5}$	$0.00024 \pm 5 \times 10^{-5}$	$0.0002 \pm 2 \times 10^{-4}$	$0.0005 \pm 1 \times 10^{-4}$	$0.0003 \pm 2 \times 10^{-4}$
honeycomb	$0.00013 \pm 6 \times 10^{-5}$	$0.0006 \pm 3 \times 10^{-4}$	$0.0004 \pm 6 \times 10^{-4}$	$0.0007 \pm 6 \times 10^{-4}$	$0.0009 \pm 3 \times 10^{-4}$

Table 4.5: Max friciton coeff

nocut	$0.0139 \pm 9 \times 10^{-4}$	$0.0083 \pm 7 \times 10^{-4}$	$0.010 \pm 1 \times 10^{-3}$	$0.0105 \pm 9 \times 10^{-4}$	
popup	$0.007 \pm 2 \times 10^{-3}$	$0.010 \pm 2 \times 10^{-3}$	$0.007 \pm 2 \times 10^{-3}$	$0.009 \pm 3 \times 10^{-3}$	$0.006 \pm 2 \times 10^{-3}$
honeycomb	$0.010 \pm 1 \times 10^{-3}$	$0.007 \pm 2 \times 10^{-3}$	$0.007 \pm 3 \times 10^{-3}$	$0.000 \pm 3 \times 10^{-3}$	$0.004 \pm 3 \times 10^{-3}$

One theory for the low friction coefficient might dependent on the fact that the normal force is only applied on the pull blocks. Especially with the cutted sheet the tension drops such that the effecive normal force on the inner sheet is not changing very much. By this theory the friction force vs. normal force on the pull blocks should look a bit more like expected and we might make some plots of thoose to check

When looking at the graphs for the PB the max friction is visually textbook linear, while the mean friction is a bit more linear but also with negativ coefficients...

4.7 Computational cost

Talk about the computatational cost of different choices. How does computation time scale with drag speed, dt and maybe T and K as well. One could also mention scaling with system size.

Show how the number of cores per simulation scale to argue that running on just one core (maybe 4) is smart for the next step of many simulations.

Mention the trouble with GPU to show that this was considered, and in fact this was the reason for choosing the Tersoff potential over the AIREBO which is perhaps more common these days...

Appendices

Appendix A

Appendix B

Appendix C

Bibliography

- ¹E. Gnecco and E. Meyer, *Elements of friction theory and nanotribology* (Cambridge University Press, 2015).
- ²Bhusnur, “Introduction”, in *Introduction to tribology* (John Wiley & Sons, Ltd, 2013) Chap. 1, 1–?
- ³H.-J. Kim and D.-E. Kim, “Nano-scale friction: a review”, *International Journal of Precision Engineering and Manufacturing* **10**, 141–151 (2009).
- ⁴K. Holmberg and A. Erdemir, “Influence of tribology on global energy consumption, costs and emissions”, *Friction* **5**, 263–284 (2017).
- ⁵B. Bhushan, “Gecko feet: natural hairy attachment systems for smart adhesion – mechanism, modeling and development of bio-inspired materials”, in *Nanotribology and nanomechanics: an introduction* (Springer Berlin Heidelberg, Berlin, Heidelberg, 2008), pp. 1073–1134.
- ⁶P. Z. Hanakata, E. D. Cubuk, D. K. Campbell, and H. S. Park, “Accelerated search and design of stretchable graphene kirigami using machine learning”, *Phys. Rev. Lett.* **121**, 255304 (2018).
- ⁷P. Z. Hanakata, E. D. Cubuk, D. K. Campbell, and H. S. Park, “Forward and inverse design of kirigami via supervised autoencoder”, *Phys. Rev. Res.* **2**, 042006 (2020).
- ⁸L.-K. Wan, Y.-X. Xue, J.-W. Jiang, and H. S. Park, “Machine learning accelerated search of the strongest graphene/h-bn interface with designed fracture properties”, *Journal of Applied Physics* **133**, 024302 (2023).
- ⁹Y. Mao, Q. He, and X. Zhao, “Designing complex architected materials with generative adversarial networks”, *Science Advances* **6**, eaaz4169 (2020).
- ¹⁰Z. Yang, C.-H. Yu, and M. J. Buehler, “Deep learning model to predict complex stress and strain fields in hierarchical composites”, *Science Advances* **7**, eabd7416 (2021).
- ¹¹A. E. Forte, P. Z. Hanakata, L. Jin, E. Zari, A. Zareei, M. C. Fernandes, L. Sumner, J. Alvarez, and K. Bertoldi, “Inverse design of inflatable soft membranes through machine learning”, *Advanced Functional Materials* **32**, 2111610 (2022).
- ¹²S. Chen, J. Chen, X. Zhang, Z.-Y. Li, and J. Li, “Kirigami/origami: unfolding the new regime of advanced 3D microfabrication/nanofabrication with “folding””, *Light: Science & Applications* **9**, 75 (2020).
- ¹³Z. Deng, A. Smolyanitsky, Q. Li, X.-Q. Feng, and R. J. Cannara, “Adhesion-dependent negative friction coefficient on chemically modified graphite at the nanoscale”, *Nature Materials* **11**, 1032–1037 (2012).
- ¹⁴R. W. Liefferink, B. Weber, C. Coulais, and D. Bonn, “Geometric control of sliding friction”, *Extreme Mechanics Letters* **49**, 101475 (2021).
- ¹⁵N Manini, O. M. Braun, E Tosatti, R Guerra, and A Vanossi, “Friction and nonlinear dynamics”, *Journal of Physics: Condensed Matter* **28**, 293001 (2016).
- ¹⁶B. Bhushan and A. V. Kulkarni, “Effect of normal load on microscale friction measurements”, *Thin Solid Films* **278**, 49–56 (1996).
- ¹⁷J. Gao, W. D. Luedtke, D. Gourdon, M. Ruths, J. N. Israelachvili, and U. Landman, “Frictional forces and amontons’ law: from the molecular to the macroscopic scale”, *The Journal of Physical Chemistry B* **108**, Publisher: American Chemical Society, 3410–3425 (2004).
- ¹⁸Y. Mo, K. T. Turner, and I. Szlufarska, “Friction laws at the nanoscale”, *Nature* **457**, 1116–1119 (2009).
- ¹⁹G. Carbone and F. Bottiglione, “Asperity contact theories: do they predict linearity between contact area and load?”, *Journal of the Mechanics and Physics of Solids* **56**, 2555–2572 (2008).

- ²⁰W. Commons, *File:asperities.svg — wikimedia commons, the free media repository*, [Online; accessed 3-February-2023], 2022.
- ²¹I. Szlufarska, M. Chandross, and R. W. Carpick, “Recent advances in single-asperity nanotribology”, *Journal of Physics D: Applied Physics* **41**, 123001 (2008).
- ²²G. Binnig, C. F. Quate, and C. Gerber, “Atomic force microscope”, *Phys. Rev. Lett.* **56**, 930–933 (1986).
- ²³S. S. Perry, “Scanning Probe Microscopy Measurements of Friction”, *MRS Bulletin* **29**, 478–483 (2004).
- ²⁴Hertz, “On the contact of elastic solids”, *Crelle’s Journal* **92**, 156–171.
- ²⁵D. Maugis, “Adhesion of spheres: the jkr-dmt transition using a dugdale model”, *Journal of Colloid and Interface Science* **150**, 243–269 (1992).
- ²⁶M. H. Müser, “Rigorous field-theoretical approach to the contact mechanics of rough elastic solids”, *Phys. Rev. Lett.* **100**, 055504 (2008).
- ²⁷B. N. J. Persson, “Theory of rubber friction and contact mechanics”, *The Journal of Chemical Physics* **115**, 3840–3861 (2001).
- ²⁸J. A. Greenwood and J. B. P. Williamson, *Contact of nominally flat surfaces*, en, 1966.
- ²⁹A. Bush, R. Gibson, and T. Thomas, “The elastic contact of a rough surface”, *Wear* **35**, 87–111 (1975).
- ³⁰B. Luan and M. O. Robbins, “The breakdown of continuum models for mechanical contacts”, *Nature* **435**, 929–932 (2005).
- ³¹Y. Dong, A. Vadakkepatt, and A. Martini, “Analytical models for atomic friction”, *Tribology Letters* **44**, 10.1007/s11249-011-9850-2 (2011).
- ³²E. Gnecco, R. Bennewitz, T. Gyalog, C. Loppacher, M. Bammerlin, E. Meyer, and H.-J. Güntherodt, “Velocity dependence of atomic friction”, *Phys. Rev. Lett.* **84**, 1172–1175 (2000).
- ³³P. Hänggi, P. Talkner, and M. Borkovec, “Reaction-rate theory: fifty years after kramers”, *Rev. Mod. Phys.* **62**, 251–341 (1990).
- ³⁴Y. Sang, M. Dubé, and M. Grant, “Thermal effects on atomic friction”, *Phys. Rev. Lett.* **87**, 174301 (2001).
- ³⁵S. Y. Krylov, K. B. Jinesh, H. Valk, M. Dienwiebel, and J. W. M. Frenken, “Thermally induced suppression of friction at the atomic scale”, *Phys. Rev. E* **71**, 065101 (2005).
- ³⁶S. Krylov and J. Frenken, “Thermal contact delocalization in atomic scale friction: a multitude of friction regimes”, English, *New Journal of Physics* **9**, 10.1088/1367-2630/9/10/398 (2007).
- ³⁷K. B. Jinesh, S. Y. Krylov, H. Valk, M. Dienwiebel, and J. W. M. Frenken, “Thermolubricity in atomic-scale friction”, *Phys. Rev. B* **78**, 155440 (2008).
- ³⁸Q. Li, Y. Dong, D. Perez, A. Martini, and R. W. Carpick, “Speed dependence of atomic stick-slip friction in optimally matched experiments and molecular dynamics simulations”, *Phys. Rev. Lett.* **106**, 126101 (2011).
- ³⁹Y. Dong, Q. Li, and A. Martini, “Molecular dynamics simulation of atomic friction: a review and guide”, *Journal of Vacuum Science & Technology A* **31**, 030801 (2013).
- ⁴⁰K. Johnson and J. Woodhouse, “Stick-slip motion in the atomic force microscope”, *Tribology Letters* **5**, 155–160 (1998).
- ⁴¹S. N. Medyanik, W. K. Liu, I.-H. Sung, and R. W. Carpick, “Predictions and observations of multiple slip modes in atomic-scale friction”, *Phys. Rev. Lett.* **97**, 136106 (2006).
- ⁴²J. Norell, A. Fasolino, and A. Wijn, “Emergent friction in two-dimensional frenkel-kontorova models”, *Physical Review E* **94**, 10.1103/PhysRevE.94.023001 (2016).
- ⁴³M. Dienwiebel, N. Pradeep, G. S. Verhoeven, H. W. Zandbergen, and J. W. Frenken, “Model experiments of superlubricity of graphite”, *Surface Science* **576**, 197–211 (2005).
- ⁴⁴C. Kittel, *Introduction to solid state physics*, 8th ed. (Wiley, 2004).
- ⁴⁵J. A. van den Ende, A. S. de Wijn, and A. Fasolino, “The effect of temperature and velocity on superlubricity”, *Journal of Physics: Condensed Matter* **24**, 445009 (2012).
- ⁴⁶B. Bhushan, “Nanotribology and nanomechanics”, *Wear* **259**, 15th International Conference on Wear of Materials, 1–? (2005).

- ⁴⁷O. Penkov, H.-J. Kim, H.-J. Kim, and D.-E. Kim, “Tribology of graphene: A review”, *International Journal of Precision Engineering and Manufacturing* **15**, 577–585 (2014).
- ⁴⁸G Paolicelli, M Tripathi, V Corradini, A Candini, and S Valeri, “Nanoscale frictional behavior of graphene on sio₂ and ni(111) substrates”, *Nanotechnology* **26**, 055703 (2015).
- ⁴⁹S. Zhang, Y. Hou, S. Li, L. Liu, Z. Zhang, X.-Q. Feng, and Q. Li, “Tuning friction to a superlubric state via in-plane straining”, *Proceedings of the National Academy of Sciences* **116**, Publisher: Proceedings of the National Academy of Sciences, 24452–24456 (2019).
- ⁵⁰M. R. Vazirisereshk, H. Ye, Z. Ye, A. Otero-de-la Roza, M.-Q. Zhao, Z. Gao, A. T. C. Johnson, E. R. Johnson, R. W. Carpick, and A. Martini, “Origin of nanoscale friction contrast between supported graphene, mos₂, and a graphene/mos₂ heterostructure”, *Nano Letters* **19**, PMID: 31267757, 5496–5505 (2019).
- ⁵¹H. M. Yoon, Y. Jung, S. C. Jun, S. Kondaraju, and J. S. Lee, “Molecular dynamics simulations of nanoscale and sub-nanoscale friction behavior between graphene and a silicon tip: analysis of tip apex motion.”, *Nanoscale* **7** **14**, 6295–303 (2015).
- ⁵²S. Li, Q. Li, R. W. Carpick, P. Gumbsch, X. Z. Liu, X. Ding, J. Sun, and J. Li, “The evolving quality of frictional contact with graphene”, *Nature* **539**, Number: 7630, 541–545 (2016).
- ⁵³A. Wijn, A. Fasolino, A. Filippov, and M. Urbakh, “Low friction and rotational dynamics of crystalline flakes in solid lubrication”, *Europhysics Letters (epl)* **95**, 10.1209/0295-5075/95/66002 (2011).
- ⁵⁴H.-J. Kim and D.-E. Kim, “Molecular dynamics simulation of atomic-scale frictional behavior of corrugated nano-structured surfaces”, *Nanoscale* **4**, 3937–3944 (2012).
- ⁵⁵X. Feng, S. Kwon, J. Y. Park, and M. Salmeron, “Superlubric sliding of graphene nanoflakes on graphene”, *ACS Nano* **7**, Publisher: American Chemical Society, 1718–1724 (2013).
- ⁵⁶F. Bonelli, N. Manini, E. Cadelano, and L. Colombo, “Atomistic simulations of the sliding friction of graphene flakes”, *The European Physical Journal B* **70**, 449–459 (2009).
- ⁵⁷M. Reguzzoni, A. Fasolino, E. Molinari, and M. C. Righi, “Friction by shear deformations in multilayer graphene”, *The Journal of Physical Chemistry C* **116**, 21104–21108 (2012).
- ⁵⁸Y. Liu, F. Grey, and Q. Zheng, “The high-speed sliding friction of graphene and novel routes to persistent superlubricity”, *Scientific Reports* **4**, 4875 (2014).
- ⁵⁹P. Zhu and R. Li, “Study of nanoscale friction behaviors of graphene on gold substrates using molecular dynamics”, *Nanoscale Research Letters* **13**, 34 (2018).
- ⁶⁰J. Zhang, E. Osloub, F. Siddiqui, W. Zhang, T. Ragab, and C. Basaran, “Anisotropy of graphene nanoflake/diamond interface frictional properties”, *Materials* **12**, 10.3390/ma12091425 (2019).
- ⁶¹M. Reguzzoni and M. C. Righi, “Size dependence of static friction between solid clusters and substrates”, *Phys. Rev. B* **85**, 201412 (2012).
- ⁶²N. Varini, A. Vanossi, R. Guerra, D. Mandelli, R. Capozza, and E. Tosatti, “Static friction scaling of physisorbed islands: the key is in the edge”, *Nanoscale* **7**, 2093–2101 (2015).
- ⁶³R. Guerra, U. Tartaglino, A. Vanossi, and E. Tosatti, “Ballistic nanofriction”, *Nature Materials* **9**, 634–637 (2010).
- ⁶⁴U. D. Schwarz, O. Zwörner, P. Köster, and R. Wiesendanger, “Quantitative analysis of the frictional properties of solid materials at low loads. i. carbon compounds”, *Phys. Rev. B* **56**, 6987–6996 (1997).
- ⁶⁵X. Zhao, M. Hamilton, W. G. Sawyer, and S. S. Perry, “Thermally activated friction”, *Tribology Letters* **27**, 113–117 (2007).
- ⁶⁶J. Tersoff, “New empirical approach for the structure and energy of covalent systems”, *Phys. Rev. B* **37**, 6991–7000 (1988).
- ⁶⁷Q. Zhang, D. Diao, and M. Kubo, “Nanoscratching of multi-layer graphene by molecular dynamics simulations”, *Tribology International* **88**, 85–88 (2015).
- ⁶⁸S. Corporation, *Pair-style lj/cut command*, (Dec. 22, 2022) https://docs.lammps.org/pair_lj.html.
- ⁶⁹X. Wang, S. Ramírez-Hinestrosa, J. Dobnikar, and D. Frenkel, “The lennard-jones potential: when (not) to use it”, *Phys. Chem. Chem. Phys.* **22**, 10624–10633 (2020).

- ⁷⁰R. Naeem, *Lennard-jones potential*, (Nov. 25, 2022) [https://chem.libretexts.org/Bookshelves/Physical_and_Theoretical_Chemistry_Textbook_Maps/Supplemental_Modules_\(Physical_and_Theoretical_Chemistry\)/Physical_Properties_of_Matter/Atomic_and_Molecular_Properties/Intermolecular_Forces/Specific_Interactions/Lennard-Jones_Potential](https://chem.libretexts.org/Bookshelves/Physical_and_Theoretical_Chemistry_Textbook_Maps/Supplemental_Modules_(Physical_and_Theoretical_Chemistry)/Physical_Properties_of_Matter/Atomic_and_Molecular_Properties/Intermolecular_Forces/Specific_Interactions/Lennard-Jones_Potential).
- ⁷¹S. Corporation, *Pair-style sw command*, (Dec. 22, 2022) https://docs.lammps.org/pair_sw.html.
- ⁷²F. H. Stillinger and T. A. Weber, “Computer simulation of local order in condensed phases of silicon”, *Phys. Rev. B* **31**, 5262–5271 (1985).
- ⁷³S. Corporation, *Pair-style tersoff command*, (Dec. 22, 2022) https://docs.lammps.org/pair_tersoff.html.
- ⁷⁴T. Schneider and E. Stoll, “Molecular-dynamics study of a three-dimensional one-component model for distortive phase transitions”, *Phys. Rev. B* **17**, 1302–1322 (1978).